A STUDY INTO PHOTOCATALYTIC DEGRADATION OF METHYLENE BLUE AND GLYCEROL AQUEOUS SOLUTION OVER COPPER FERRITE CATALYST

LUM SIN WAN

BACHELOR OF CHEMICAL ENGINEERING
UNIVERSITI MALAYSIA PAHANG

Thesis Access Form

No_____Location_____

Author : ……

Title : ……

Status of access OPEN / RESTRICTED / CONFIDENTIAL

Moratorium period:_____ years, ending_____/_____200____

Conditions of access proved by (CAPITALS): DR CHENG CHIN KUI

Supervisor (Signature)……

Faculty: ……

Author's Declaration: *I agree the following conditions:*

OPEN access work shall be made available in the Universiti Malaysia Pahang only and not allowed to reproduce for any purposes.

*The statement itself shall apply to **ALL** copies:*

This copy has been supplied on the understanding that it is copyright material and that no quotation from the thesis may be published without proper acknowledgement.

Restricted/confidential work: All access and any photocopying shall be strictly subject to written permission from the University Head of Department and any external sponsor, if any.

Author's signature…….Date: ……

users declaration: for signature during any Moratorium period (Not Open work): ***I undertake to uphold the above conditions:***			
Date	Name (CAPITALS)	Signature	Address

A STUDY INTO PHOTOCATALYTIC DEGRADATION OF METHYLENE BLUE AND GLYCEROL AQUEOUS SOLUTION OVER COPPER FERRITE CATALYST

LUM SIN WAN

Thesis submitted in partial fulfilment of the requirements
for the award of the degree of
Bachelor of Chemical Engineering

Faculty of Chemical & Natural Resources Engineering
UNIVERSITI MALAYSIA PAHANG

Jan 2015

SUPERVISOR'S DECLARATION

I hereby declare that I have checked this thesis and in my opinion, this thesis is adequate in terms of scope and quality for the award of the degree of Bachelor of Chemical Engineering.

Signature	:
Name of main supervisor	: DR. CHENG CHIN KUI
Position	: SENIOR LECTURER
Date	: 31/12/2014

STUDENT'S DECLARATION

I hereby declare that the work in this thesis is my own except for quotations and summaries which have been duly acknowledged. The thesis has not been accepted for any degree and is not concurrently submitted for award of other degree.

Signature :
Name : LUM SIN WAN
ID Number : KA11096
Date : 31/12/2014

Dedication

To myself

ACKNOWLEDGEMENT

I would like to take this opportunity to express my profound gratitude and deep regards to Dr. Cheng Chin Kui for his exemplary guidance, monitoring and constant encouragement throughout the course of this thesis. The blessing, help and guidance given by him time to time shall carry me a long way in the journey of life on which I am about to embark.

I wish to thank my colleague, Tan Sze Yee for her companionship and moral support in completing this research.

ABSTRACT

There is a growing concern on environmental damage arising from industrial discharge such as organic dyes from textile, paper, printing and leather sectors as well as glycerol waste from biodiesel sector. Consequently, this has generated a genuine interest to use catalytic green pathway to treat these effluents, hence the motivation behind the current work. In the current work, the photocatalyst employed was copper ferrite ($CuFe_2O_4$), which was prepared via co-precipitation method. Subsequently, the physicochemical properties of $CuFe_2O_4$ were examined using gas pycnometer, N_2 physisorption to obtain Brunauer-Emmett-Teller (BET) specific surface area, Field Emission Scanning Electron Microscope (FESEM) and X-ray Diffraction (XRD). The effects of photocatalyst on the photo-degradation of 20 ppm methylene blue solution under visible light were examined over catalyst loadings of 0.5 and 1.0g/L. From the result, it can be concluded that $CuFe_2O_4$ was effective in the photo-degradation of methylene blue solution for both the catalyst loading of 0.5 and 1.0g/L. In addition, the photo-degradation of 0.5 v/v% glycerol solution was carried out with a catalyst loading of 2.0 g/L. The 2.0 g/L of $CuFe_2O_4$ was not effective in the glycerol solution. However, when H_2O_2 was added, a photo-fenton system was created and it has degraded the glycerol. The amount of hydrogen peroxide (H_2O_2) was therefore varied to determine the effectiveness of photo-fenton system of the catalyst in the photo-degradation of glycerol solution. The best amount of H_2O_2 for the glycerol solution-$CuFe_2O_4$ was 1.0 ml as it exhibited superior glycerol decomposition.

Keywords: Copper ferrite; Glycerol; Methylene blue; Photocatalysis; Visible light

ABSTRAK

Kerosakan alam sekitar telah berpunca daripada pelepasan perindustrian seperti pewarna organik dari sektor tekstil, kertas, percetakan dan juga sisa gliserol dari sektor biodiesel. Oleh yang demikian, hal ini telah menjana minat yang tulus untuk menggunakan laluan hijau pemangkin untuk merawat efluen ini, iaitu motivasi kerja ini. Pemangkin yang akan diguna ialah kuprum ferit ($CuFe_2O_4$) melalui kaedah "co-precipitation". Di samping itu, sifat-sifat fizikokimia $CuFe_2O_4$ akan diperiksa menggunakan piknometer gas, kaedah penyerapan fizikal cecair N_2, Brunauer-Emmett-Teller (BET) untuk mendapatkan kawasan permukaan, Imbasan Elektron Mikroskop (FESEM) dan sinar X-ray (XRD). Kesan fotomangkin ke atas foto-penguraianlarutan Metilena biru dalam 20 ppm di bawah cahaya visible telah diperiksa dengan pemangkin 0.5 dan 1.0 g/L. Daripada keputusan itu, dapat disimpulkan bahawa $CuFe_2O_4$ berkesan dalam foto-penguraianlarutan Metilena biru untuk kedua-dua pemangkin iaitu 0.5 dan 1.0 g/L. Selain itu, foto-penguraianlarutan dalam 0.5 v/v% gliserol telah dijalankan dengan pemangkin sebanyak 2.0 g/L. $CuFe_2O_4$ dalm 2.0 g/L tidak berkesan dalam foto-penguraianlarutan gliserol. Walau bagaimanapun, apabila H_2O_2 ditambah, sistem foto-Fenton telah dicipta dan ini telah menguraianlarutan gliserol. Jumlah hidrogen peroksida (H_2O_2) telah diubah untuk menentukan keberkesanan sistem foto-Fenton dalam foto-penguraianlarutan gliserol. Jumlah optimum hidrogen peroksida ditambah dalam larutan gliserol dengan $CuFe_2O_4$ ialah 1.0 ml. Ini telah menunjukkan prestasi foto-penguraianlarutan terbaik.

Kata Kunci: kuprum ferit; gliserol; fotopemangkinan; Metilena biru; cahaya visible

TABLE OF CONTENTS

LIST OF FIGURES

LIST OF TABLES

CHAPTER 1

1 INTRODUCTION

1.1 Motivation and statement of problem

Today, the increase of human population and growing industrialization have culminated in the discharge of different pollutants to the environment. Indeed, wastewater from the textile, paper, rubber, plastics, cosmetics, and pharmaceutical and food industries contains dye stuffs, suspended solids, other soluble organic substances, and heavy metals which will contaminate the water source (Fan et al., 2014). Most of these contaminants especially dyes, exist in industrial wastewater and even our drinking water system, which are extremely dangerous to the environment and human-kind due to their toxicity and resistance to natural degradation. Furthermore, light penetration in water will be hindered and photosynthesis in aquatic plants will be disrupted in the presence of dyes. More importantly, this will kill aquatic life and hence affect the ecosystem (Khosravi & Eftekhar, 2014). On top of that, dyes are hazardous pollutants which can modify the physical and chemical properties of any ecosystem.

The current dyeing process is toxic and wasteful. The process can release polluted water and chemicals. There are more than 100,000 different synthetic dyes available on the market, produced in over 700,000 tons annually worldwide (Adedayo et al., 2004). In the textile industry alone, up to 200,000 tons of these dyes are lost to effluents every year during the dyeing process. This is due to the inefficiency of the dyeing process. Most of these dyes escape conventional wastewater treatment processes and stay in the environment as a result of their high stability to light, temperature, water, detergents, chemicals, soap and other parameters (Ogugbue & Sawidis, 2011). Due to the reasons mentioned above, wastewater from textile plants is termed as the most polluting by taking into account of the volume generated and also the effluent composition among all the other industrial sectors. Subsequently, dyes wastewater has contributed to severe pollution problems at present (Chequer et al., 2013).

For the case of glycerol waste, according to Yusuf et al. (2011), the world biodiesel capacity in the year 2010 is 15000 million litres, a jump from 9000 million litres recorded in 2009. Moreover, the report prepared by National Biodiesel Board indicated that there are 105 biodiesel production facilities operating in the United States in 2007 and 77 other facilities are in the planning or construction stage. In addition, the annual biodiesel consumption in the United States has been growing at a rate of 30–50% per year from 15 billion litres in 2006. It is expected to achieve an annual target of 30 billion litres at the end of year 2012 (Ayoub & Abdullah, 2012). This implies that the production of biodiesel has increased dramatically; hence generation of glycerol as by-product from transesterification also increased significantly. Generally, 10 kg of glycerol is produced for every 100 kg of biodiesel, or in other words, an approximately 10% of glycerol by volume is generated during the production of biodiesel (Leoneti et al., 2012).

As the demand for biodiesel incrementally increases, the market is expected to be inundated with crude glycerol. Therefore, there is a need to promote alternative use of the excess glycerol, either to convert or purify it into some conventional materials that can be used for food, cosmetics or drugs sectors. Alarmingly, the discharge of untreated glycerol can cause serious environmental issues. Specifically in Malaysia, glycerol is classified as waste under Schedule S181 of the Environmental Regulations and stored in drums and disposed in landfills (Yong et al., 2001). The excess glycerol can be used for the production of chemical products, fuel additives, production of hydrogen, development of fuel cells, etc (Leoneti et al., 2012).

Therefore, there is a growing concern on environmental damage arising from industrial discharge such as organic dyes as well as glycerol waste from biodiesel sector. These two concerns motivate the current work to explore the potential of employing photocatalysis to degrade methylene blue and glycerol solution. The chosen catalyst, copper ferrite ($CuFe_2O_4$), is capable of performing photocatalytic conversion of visible solar energy (wavelength range from 400 to 700 nm) to generate e^-/h^+ on photocatalytic surface. The e^-/h^+ pairs are involved in the pathway towards hydroxyl radical generation which is critical for the decomposition of the contaminants. To enhance the generation of hydroxyl radical, Fenton-type system was also created by adding hydrogen peroxide (H_2O_2). This system was created in which iron cations react with H_2O_2, thereby enhancing the production of reactive oxygen species such as radicals (Casbeer et al., 2012).

1.2 Objectives

The current work is aimed at synthesizing, characterizing the physicochemical properties and evaluating the photocatalytic performance of copper ferrite ($CuFe_2O_4$) for photo-degradation of methylene blue and glycerol solution.

1.3 Scopes of study

In order to achieve the outlined objectives of the current work, the following scopes have been identified:

I. To synthesize ($CuFe_2O_4$) photocatalyst using co-precipitation method employing metal loading of 30 wt%.

II. To characterize the physicochemical properties of ($CuFe_2O_4$) photocatalyst using spectroscopic analyses such as:

   a) FESEM
   b) Gas pycnometer
   c) Nitrogen physisorption (Brunauer-Emmett-Teller, BET)
   d) X-ray diffraction (XRD)

III. To study the photo-degradation of methylene blue and glycerol solution. The effect of Fenton system in the photo-degradation also being studied.

1.4 Novelty of work

The current work serves to explore the potential of employing photocatalyst to photo-degrade methylene blue and glycerol solution. The chosen photocatalyst, copper ferrite ($CuFe_2O_4$) is capable in photocatalytic conversion of visible solar energy to generate e^-/h^+, which in turn produce reactive oxygen species through redox processes. The photocatalytic process can be enhanced in a Fenton type system in which iron cations react with H_2O_2 thereby enhance the production of reactive oxygen species such as radicals to further aid in the photo-degradation of methylene blue and glycerol solution.

1.5 Outline of Thesis

The structure of the reminder of the thesis is outlined as follow:

Chapter 2 provides a description of the mechanism of the photocatalyst as well as photocatalysis of methylene blue and glycerol solution. It explains how the photocatalyst worked in the methylene blue and glycerol solution by harnessing light energy (visible light). Physical and chemical properties of methylene blue, glycerol and copper ferrite as photocatalyst are discussed. In addition, photo-fenton system is also discussed. A summary of previous works regarding photocatalytic activity are also presented.

Chapter 3 provides a review of the preparation method of photocatalyst by using co-precipitation method. List of chemicals and equipment for characterization in this research are included in this chapter. Each of the photocatalyst characterization techniques is discussed as well.

Chapter 4 presents result and discussion in this research work. The result obtained from the experiment which is photocatalytic activity testing with methylene blue and glycerol solution is discussed thoroughly.

Conclusion and recommendation are presented in Chapter 5. A summary of this research work is covered in this chapter.

CHAPTER 2

2 LITERATURE REVIEW

2.1 Introduction

This Chapter provides a description of photocatalysis, its mechanism of the photocatalyst as well as photocatalytic of methylene blue and glycerol solution. It explains how the photocatalyst works in the methylene blue and glycerol solution by harnessing light energy. The photo-fenton system will be discussed too, in addition to the physical and chemical properties of methylene blue, glycerol and copper ferrite as photocatalyst. Finally, a summary of previous works regarding photocatalytic activity is presented.

2.2 Photocatalysis

Photocatalysis can be defined as the acceleration of a photoreaction in the presence of a catalyst (Ohama & Gemert, 2011). Photocatalysis has enormous potential to treat organic contaminants in water and air (Umar & Abdul Aziz, 2013). Consequently, it becomes a new promising approach to address the environmental problem such as the degradation of potentially toxic and dangerous contaminants from water including organic dyes and waste. It is also applied in many other applications including odour control, air purification, sterilization and cancer therapy, water splitting to produce hydrogen gas, inactivation of cancer cell and etc. The removal of contaminants such as organic dyes involve transferring the compounds between phases or from the source to treatment facilities. Ideally, the contaminants can be degraded photocatalytically into carbon dioxide and water. Furthermore, this can be done without additional waste or by-products (Casbeer et al., 2012).

2.3 Mechanism of Photocatalysis

Oxidation and reduction reactions are carried out by photocatalysts activated by light energy (hv). An electron (e^-) is excited from the valence band (VB) to the conduction band (CB) of the photocatalyst when irradiated with light energy and thus leaving a

photogenerated hole (h^+). At this stage, the energy difference between the valence band and conduction band is known as "band gap". Figure 2-1 describes the process of a photocatalyst absorbing light energy in order to produce pairs of $e^-$and h^+. Oxidation and reduction processes can occur with the produced e^-/h^+ pairs. When photocatalytic process occurs in an aqueous solution, water and hydroxide ions react with photogenerated h^+ to form hydroxyl radicals (·OH), which is the primary oxidant in the photocatalytic oxidation of organic compounds (Casbeer et al., 2012).

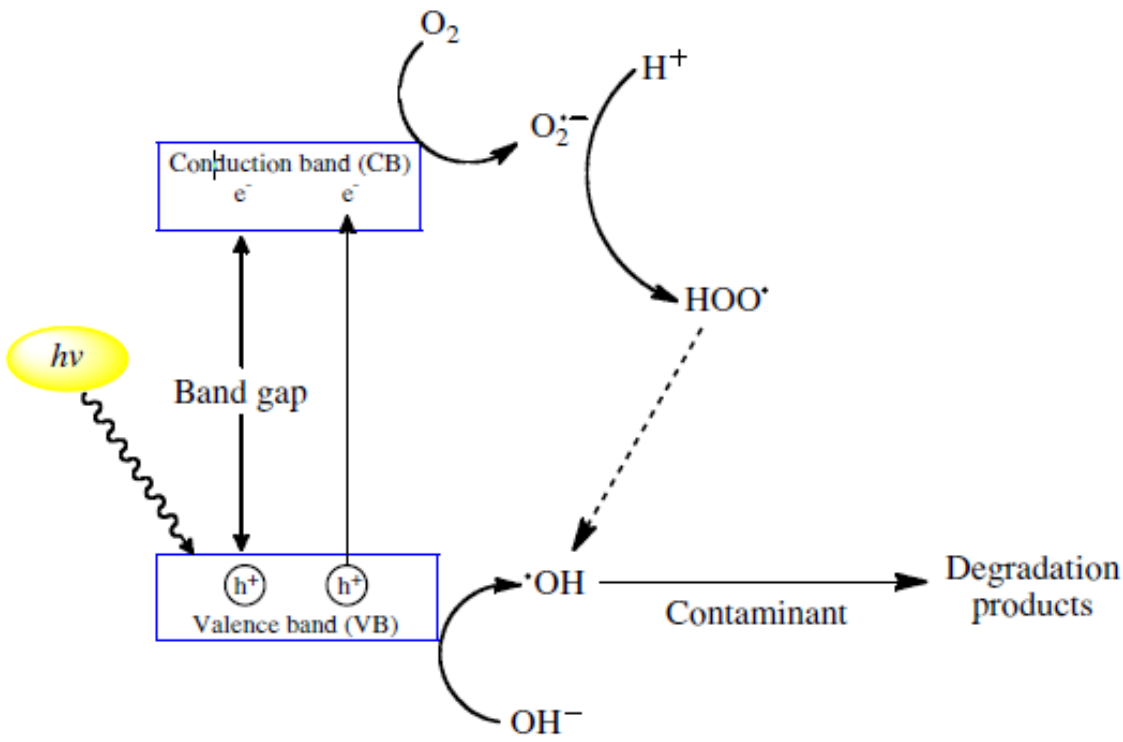

Figure 2-1: Schematic of reactions occurring via photocatalysis (Casbeer et al., 2012)

In photocatalysis, the catalyst may accelerate the photoreaction by interaction with the substrate in its ground state or excited state depending on the specific photoreaction. A sensitized photoreaction is occur when the light is adsorbed by the catalyst (C). This may occur via two different ways which are through energy transfer or electron transfer. In energy transfer, it is by forming an activated state of the reactant of interest, *S*, which is more easily oxidized than their ground state. The reaction is as follow:

$$C \xrightarrow{hv} * C \qquad (2\text{-}1)$$

$$*C + S \rightarrow *S + C \qquad (2\text{-}2)$$

$$*S \rightarrow P \qquad (2\text{-}3)$$

The second way is via electron transfer, it is by acting either as an electron acceptor or donor.

$$\mathrm{C} \xrightarrow{\mathrm{hv}} *\mathrm{C} \qquad (2\text{-}4)$$

$$*C + S \rightarrow S^{-} + C^{+} \qquad (2\text{-}5)$$

$$S^{-} \rightarrow P^{-} \qquad (2\text{-}6)$$

$$P^{-} + C^{+} \rightarrow \mathrm{P} + \mathrm{C} \qquad (2\text{-}7)$$

The product, P, is formed from the activated substrate along the potential energy curve for the case of energy transfer. In the case of electron transfer, a new reaction path is opened when the photosensinizer transfer an electron to the substrate (Ohama & Gemert, 2011).

2.4 Fenton system

Photo-Fenton system is gaining popularity and is widely used in the advanced oxidation process (AOP) for the degradation of organic pollutants (Thanh-Thuy et al., 2013). Fenton system is established when ferrite cations react with hydrogen peroxide, H_2O_2. The H_2O_2, which act as an oxidizing agent, is capable to produce free radicals from water molecules, namely $^{\cdot}OH$ and $^{\cdot}OOH$ (reactive oxygen species) when added in a reaction mixture. This Fenton system (comprised of H_2O_2/Fe_2O_3) is capable to enhance the production of reactive oxygen species and hence further aid in the degradation of contaminants. The reaction can be illustrated by the equations (Casbeer et al., 2012):

$$Fe^{2+} + H_2O_2 \rightarrow Fe^{3+} + OH^{-} + {}^{\cdot}OH \qquad (2\text{-}8)$$

$$Fe^{2+} + H_2O_2 \rightarrow Fe^{2+} + {}^{\cdot}OOH + H^{+} \qquad (2\text{-}9)$$

$$H_2O_2 + {}^{\cdot}OH \rightarrow H_2O + {}^{\cdot}OOH \qquad (2\text{-}10)$$

$$H_2O_2 + e^{-} \rightarrow OH^{-} + {}^{\cdot}OH \qquad (2\text{-}11)$$

$$OH^{-} + h^{+} \rightarrow H^{+} + {}^{\cdot}OH \qquad (2\text{-}12)$$

Photo-fenton system was first introduced in 1960s and remain until today. It is the most applied AOP and is proven for its ability to degrade organic waste by the free hydroxyl radicals produced and hence is greatly used in the treatment of wastewater. The production of free hydroxyl radicals can speed up the reaction by providing readily available binding sites during the photocatalytic degradation of organic dyes and waste (Ding et al., 2014). It can degrade high loading of organic compounds in highly saline conditions. H_2O_2 will form free hydroxyl radicals when it decomposed by Fe^{2+} ions that present in the aqueous solution even in the condition of no light irradation. However, in the presence of light source, the photo-Fenton system is expedited which should result in the rapid formation of free hydroxyl radicals from H_2O_2 decomposition by ferrous or ferric ions. All these soluble iron hydroxy or iron complexes can absorb not only ultra-violet (UV) radiation but also visible light. Photo-fenton system can react up to a light wavelength of 600 nm. The rate of a photo-fenton system was proved to be relatively higher when there is light irradiation compared to the condition in the absence of light source. This is due to the regeneration of Fe^{2+} from the photochemical effect of light source and the concurrent formation of the hydroxyl radicals in the reaction. The system can be substantial because of the cycle that keep generating hydroxyl radicals by Fe^{2+} (Chong et al., 2010).

In photo-Fenton system, further increase in the amount of H_2O_2 concentration above certain limits (critical concentration) or exceed the optimum level, it will not increase the rate of photo-degradation. According to Mohabansi et al. (2011), high concentration of hydroxyl peroxides will act as scavenger itself. This will result in the decreasing of the concentration of hydroxyl free radicals and thus reducing the efficiency in the photo-degradation rate. As a result, H_2O_2 should be added at an optimum concentration to achieve the best photo-degradation to prevent it acts as a hydroxyl radical scavenger instead of a free-radical generator (Banat et al., 2005).

Photo-Fenton system has higher photoactivity than the heterogeneous photocatalysis. However, the performance is largely dependent on water quality parameters. The generation of highly photoactive iron complexes is highly accounting on water pH and ions content (De Laat et al., 2004). It was claimed that the optimum pH for photo-fenton reaction is at 2.8. This is due to the reason that precipitation does not occur which promotes the formation of dominant iron species of $[Fe(OH)]^{2+}$ (Pignatello et al., 1992).

2.5 Methylene blue

About 15% of the total world production of dyes is lost during the dyeing process and is discharged as textile effluents. The release of those coloured dyes in wastewaters has disrupt the ecosystem (Lachheb et al., 2002). Methylene blue is one of the most well-known organic dyes and contributes to the dye pollution in water source. Therefore, it was taken as the photocatalytic reactant model in this work. Methylene blue is a heterocyclic aromatic organic compound. Its chemical formula is $C_{16}H_{18}N_3SCl$ and structural formula is shown in Figure 2-2. It appear as solid, odourless and dark green powder which will form a blue solution when dissolved in water. There are some chemical and physical properties of methylene blue which are tabulated in Table 2-1.

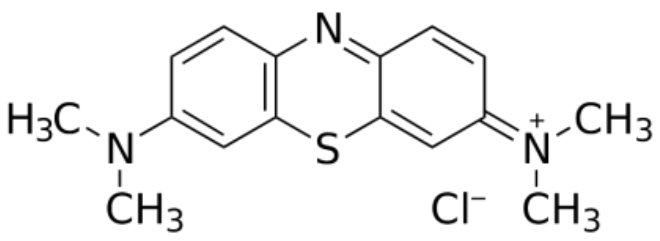

Figure 2-2: Structure of Methylene Blue (Wang et al.,2005)

Table 2-1: Some physical and chemical properties of methylene blue (MATERIAL SAFETY DATA SHEET , 2013)

Appearance	Dark greenish, hygroscopic crystalline powder
Odour	Almost odourless
Melting point	190 °C
Boiling point	Decomposes
Specific gravity	1.23
PH value	3-5 (1% aqueous solution)

2.6 Glycerol

Biodiesel, which is a kind of "safe, clean and high-efficient" energy, has high combustion efficiency. In recent years, large surplus of crude glycerol is produced as the main by-product in the production of biodiesel with the rapid development of biodiesel industry

through transesterification process. Figure 3 describes the transesterification reaction of biodiesel production Therefore, there are more and more attention has been drawn from researchers over the world on transforming glycerol to high value-added products. The transesterification reaction of biodiesel production can be represented as (Tan et al., 2013):

$$\begin{matrix} CH_2COOR_1 \\ CHCOOR_2 \\ CH_2COR_3 \end{matrix} + 3CH_3OH \xrightarrow{\text{catalyst}} \begin{matrix} COOCH_3R_1 \\ COOCH_3R_2 \\ COOCH_3R_3 \end{matrix} + \begin{matrix} CH_2OH \\ CHOH \\ CH_2OH \end{matrix} \quad (2\text{-}13)$$

$$\text{Triglycerides} + \text{Methanol} \xrightarrow{\text{catalyst}} \text{Methyl esters} + \text{Glycerine}$$

Glycerol which shown in Figure 2-3, also known as glycerine or propane-1,2,3-triol, is a clear, colourless, odourless, hygroscopic, vicious and sweet taste liquid. The boiling point, melting point and flash point of glycerol are 290°C, 18°C and 177°C, respectively. Glycerol has a molecular weight of 92.09 g/mol, a density of 1.261 g/cm^3, and a viscosity of 1.5 Pa.s under normal atmospheric pressure (Tan et al., 2013).

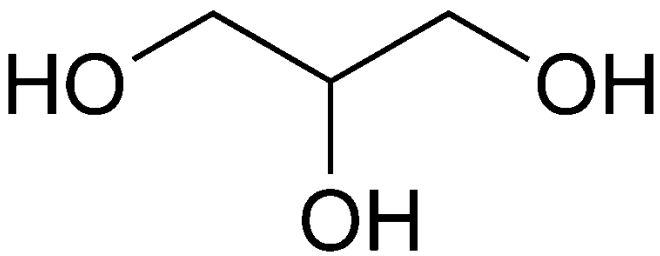

Figure 2-3: Structure of glycerol (Leoneti et al., 2012)

Generally, glycerol can be produced via chemical synthesis or microbial fermentation from petrochemical feedstocks or can be recovered as a by-product of soap manufacture from fats. Glycerol is produced as a by-product of the hydrolysis of fats in soap and other related materials in a traditional way. However, today, this process is of lesser importance as detergents has already replace soap (Wang et al., 2001). According to Prescott & Dunn

(1959), glycerol was produced through the fermentation pathway for the first time on a large scale using the sulfite-steered yeast process during World War I when the demand for glycerol in explosive manufacture far more than the supply from the soap industry.

In terms of application, glycerol is refined in an expensive process and can be used in the chemical, textile, pharmaceutical and food industries. On the other hand, there are alternatives for the use of unrefined glycerol such as production of chemical products, production of hydrogen, fuel additives and etc. Figure 2-4 shows the summary percentage for industrial applications of glycerol (Tan et al., 2013).

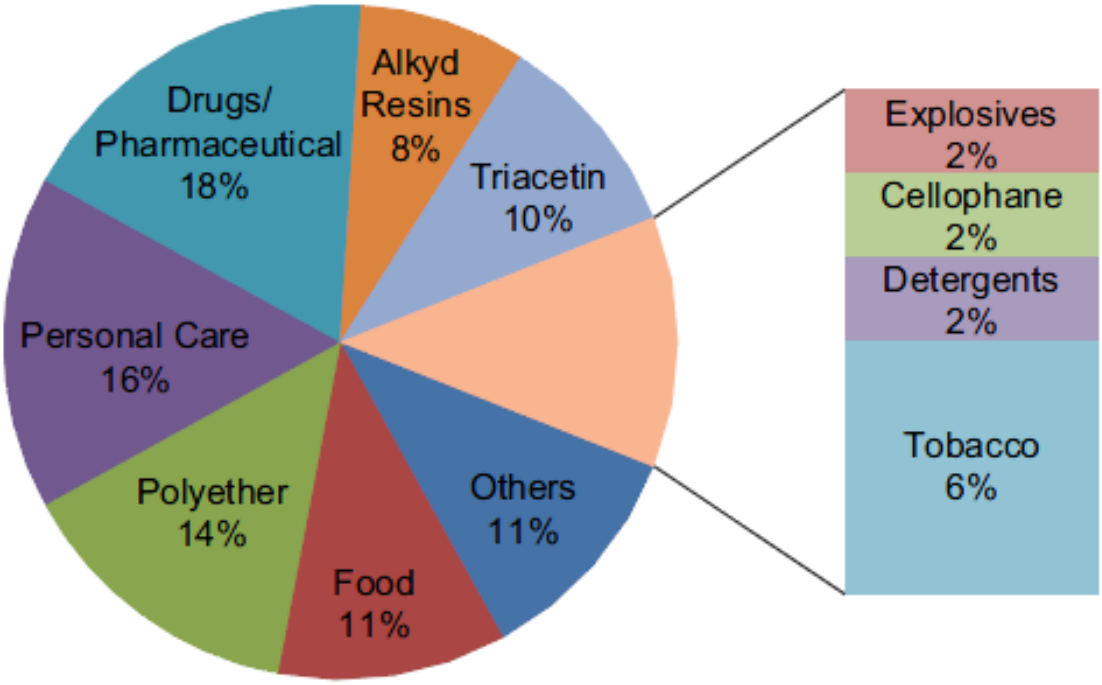

Figure 2-4: Industrial applications of glycerol (Tan et al., 2013)

2.7 Copper Ferrite as Photocatalyst

Photocatalyst, is defined as a substance which is activated by adsorbing a photon and is able to accelerate a reaction without being consumed (Umar & Abdul Aziz, 2013). Photocatalyst provides pathway for the conversion of solar energy such as UV light, visible light and infrared etc. for the use in oxidation and reduction processes. In recent years, ferrites as photocatalyst have attracted a lot of interest and attention. Unlike Titanium dioxide (TiO_2) which has been used for a long time, ferrite is unique owing to

its magnetic property. Consequently, it can be easily separated from the reaction mixture post-photocatalytic reaction. Moreover, band gap is one of the factors that need to be taken into consideration when employed as photocatalyst. Narrow band gap allows for the photocatalytic activity under visible light irradiation which has the wavelength of 400-700nm and accounts for 46% of solar energy. Figure 2-5 shows the solar energy spectrum. Copper ferrite has gained significant attention in recent years among other ferrites. The distribution of cations in this structure can be represented by $[Cu_x^{2+}Fe_{1-x}^{3+}]_A[Cu_{1-x}^{2+}Fe_{1+x}^{3+}]_BO_4$. The parameter of inversion, x, is equal to 0 for inverse spinels, and x is equal to 1 when the spinel is normal. The distribution of the cations has significant effects on the crystal symmetry and the properties of these ferrites, depending on the method of preparation such as sol gel method, co-precipitation, combustion synthesis, emulsion-assisted hydrothermal methods and etc. based on the preparation method, $CuFe_2O_4$ can crystallize either in tetragonal or cubic symmetry (Naseri et al., 2013). Copper ferrite has a relatively narrow band gap which is 1.32 eV as can be observed from Table 2-2. In addition, copper ferrite is a chemically and thermally stable magnetic material that has been used in many other areas. Ferrites have many important photocatalytic properties for industrial processes, such as the oxidative dehydrogenation of hydrocarbons, the oxidation of CO, H_2, CH_4, alkylation reactions, etc (Casbeer et al., 2012). On top of that, size and sturucture of the photocatalyst will affect the performance of degradation of organic compounds. Surface morphology includes particle size and agglomerate size, is an important factor that needed to be taken into consideration in photocatalytic degradation process. There is a direct relationship between surface coverage of the photocatalyst as well as organic compounds. The rate of photocatalytic reaction will be governed by the number of photon striking the photocatalyst. This implies that the reaction happen only in the absorbed phase of the photocatalyst (Kogo et al., 1980).

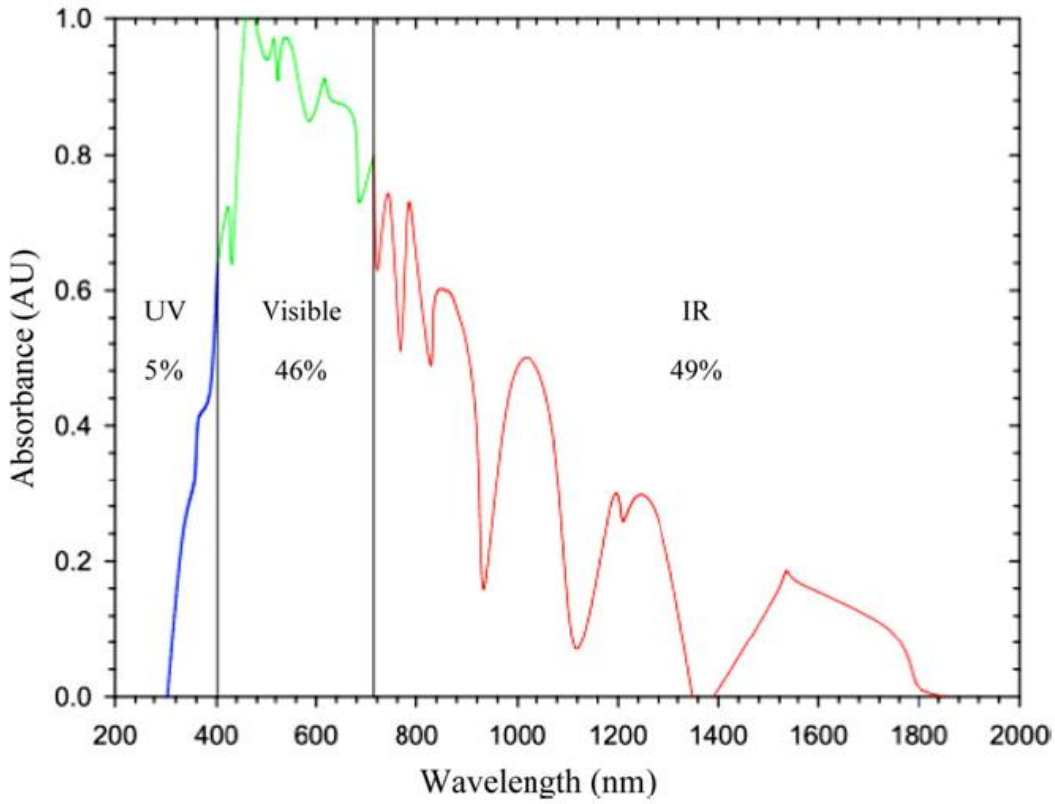

Figure 2-5: Solar energy spectrum (Casbeer et al., 2012)

Table 2-2: Band gap energy for selected photocatalysts (Casbeer et al.,2012)

Ferrite	Band gap (eV)
$CaFe_2O_4$	1.9
$MgFe_2O_4$	2.18
$ZnFe_2O_4$	1.92
$NiFe_2O_4$	2.19
$CuFe_2O_4$	1.32
$SrTiO_3$	3.5
TiO_2	3.2
Fe_2O_3	2.3
ZnS	3.6
CdS	2.4
WO_3	2.8
Ag_3VO_4	2.2

2.8 Photocatalysis of Glycerol

In recent years, glycerol has been used to produce hydrogen from different methods such as steam reforming, gasification, autothermal reforming, aqueous-phase reforming, electrochemical reforming, photo fermentation and supercritical water reforming processes. The majority of studies on hydrogen production from glycerol have focused on thermochemical routes. However, hydrogen can be produced from biomass in ambient conditions (temperature and pressure) via a photocatalytic route, which is an efficient, ecologically benign and low-cost process. This technology is based on photo electrochemical cells operating with two redox systems.

Kondarides et al (2008) have done a lot of experiments on variety of biomass-derived components, including monosaccharides and hexoses, alcohols and organic acids. From the experimental results, the amounts of H_2 and CO_2 produced were found to be in the following general reforming reaction:

$$C_xH_yO_z + (2x - \mathbf{z})\ H_2O \rightarrow xCO_2 + (2x - z + y/2)\ H_2 \qquad (2\text{-}14)$$

The production of hydrogen and oxygen by water cleavage from glycerol occurs under non-aerated conditions and is attained by photo-generated electrons and holes, respectively, in a condition that their energy is sufficient to reduce protons toward hydrogen molecules and to oxidize water toward oxygen. From another aspects, the photocatalytic oxidation of glycerol takes place in the presence of oxygen with the participation of photo-generated holes, which act either directly or indirectly by generating hydroxyl radicals (·OH), which then lead to the production of CO_2 and H_2O. In this case, photo-generated electrons are consumed by chemisorbed oxygen to form superoxide radicals ($\cdot O_2^-$). In a photo-induced reforming process, the two reactions are combined, which is the photocatalytic treatment of glycerol solution and derivatives takes place under non-aerated conditions. This results in the oxidation of the organic substrate by holes toward CO_2, which is accompanied by production of gas-phase hydrogen from water, while the oxidation of water reaction and the formation of superoxide radicals are suppressed (Melo & Silva, 2011).

For glycerol photo-reforming, the reaction can be shown as:

$$C_3H_8O_3 + 3H_2O \rightarrow 3CO_2 + 7H_2 \quad (2\text{-}15)$$

For glycerol photo-oxidation, the reaction can be shown as follows:

$$C_3H_8O_3 + (7/2)\ H_2O \rightarrow 3CO_2 + 4H_2 \quad (2\text{-}16)$$

2.9 Photo-degradation of Organic Dyes

A large amount of effort has been devoted over the years for developing heterogeneous photocatalysts with high activities for environmental applications including air purification, water disinfection, hazardous waste remediation, and water purification. Titania has proven to be the most suitable for widespread environmental applications among various oxide semiconductor photocatalysts (Yu et al., 2002). However, two main drawbacks which are low quantum efficiency due to the high recombination rate of photo-induced electron–hole pairs (e^-&h^+) and poor absorption ability in the visible-light region, has limit the efficiency of TiO_2 photocatalytic reactions (Yang et al., 2010). Thus, a great deal of effort has been made to increase the photocatalytic activity of the photocatalyst. A lot of organic matters can be decomposed into inorganic and low-toxicity smaller compound through photocatalysis process (Meng & Juan, 2008).

Tables 2-3, 2-4, and 2-5 as well as Figure 2-6 show the previous photocatalytic work of ferrites in degrading different concentrations of dyes,with different catalyst loading, irradiation source and irradiation time with the respective degradation in percentage. Table 2-3 summarizes some works related to the use of ferrites and mixed ferrites for photocatalyzing methylene blue while Table 2-4 shows works pertaining to ferrites and mixed ferrites with Rhodamine B dye. Table 2-5 shows some reaction of various dyes with ferrites and H_2O_2 in the absence of light irradiation. On the other hand, Figure 2-6 shows the degradation of methylene blue and Rhodamine B dyes by $TiO_2/ZnFe_2O_4$ composite photocatalysts.

Table 2-3: Ferrites and mixed ferrites reacted with methylene blue dye (Casbeer et al.,2012)

Photocatalyst	Dye (mg/L)	Catalyst loading (g/L)	Irradiation source	Irradiation time (min)	Degradation (%)
$BaFe_2O_4$	20	5	UV	120	65
$TiO_2/CoFe_2O_4/SiO_2$	6	n/a	UV	250	60
TiO_2 /$CoFe_2O_4$	6	n/a	UV	250	0
$CoFe_2O_4/ZnO$	50	30	UV	300	93.9
$SiO_2/NiFe_2O_4$	10	1.0	$\lambda > 400$ nm	60	5
$Bi_{12}TiO_2/NiFe_2O_4$	10	1.1	$\lambda > 400$ nm	60	52
SiO_2/ $NiFe_2O_4$	10	1.1	$\lambda > 400$ nm	30	85
$Bi_{12}TiO_20$/ SiO_2/ $NiFe_2O_4$	10	1.1	$\lambda > 400$ nm	240	18
TiO_2/ $NiFe_2O_4$	8	0.8	UV	420	80
$TiO_2/ZnFe_2O_4$	10	5	$\lambda > 400$ nm	180	5
$ZnFe_2O_4$	25	5	$\lambda > 400$ nm	240	4

Table 2-4: Ferrites and mixed ferrites reacted with Rhodamine B dye (Casbeer et al.,2012)

Photocatalyst	Dye conc. (mg/L)	Catalyst loading (g/L)	Irradiation time (min)	Irradiation source	Degradation (%)
$ZnFe_2O_4$	10	2.0	150	200-700 nm	60
$ZnFe_2O_4$/Ag (8.1%)	10	2.0	150	200-700 nm	95
$ZnFe_2O_4$/Ag (22.7%)	10	2.0	150	200-700 nm	98
$TiO_2/ZnFe_2O_4$	9.6	1	150	λ =254nm	99.7
Ag/ Fe_3O_4/ SiO_2	25	0.5	150	$\lambda > 420$ nm	10
AgI/ Fe_3O_4/ SiO_2	25	0.5	150	$\lambda > 420$ nm	20
$BaFe_2O_4$/ SiO_2/ TiO_2	10	0.8	80	UV	59

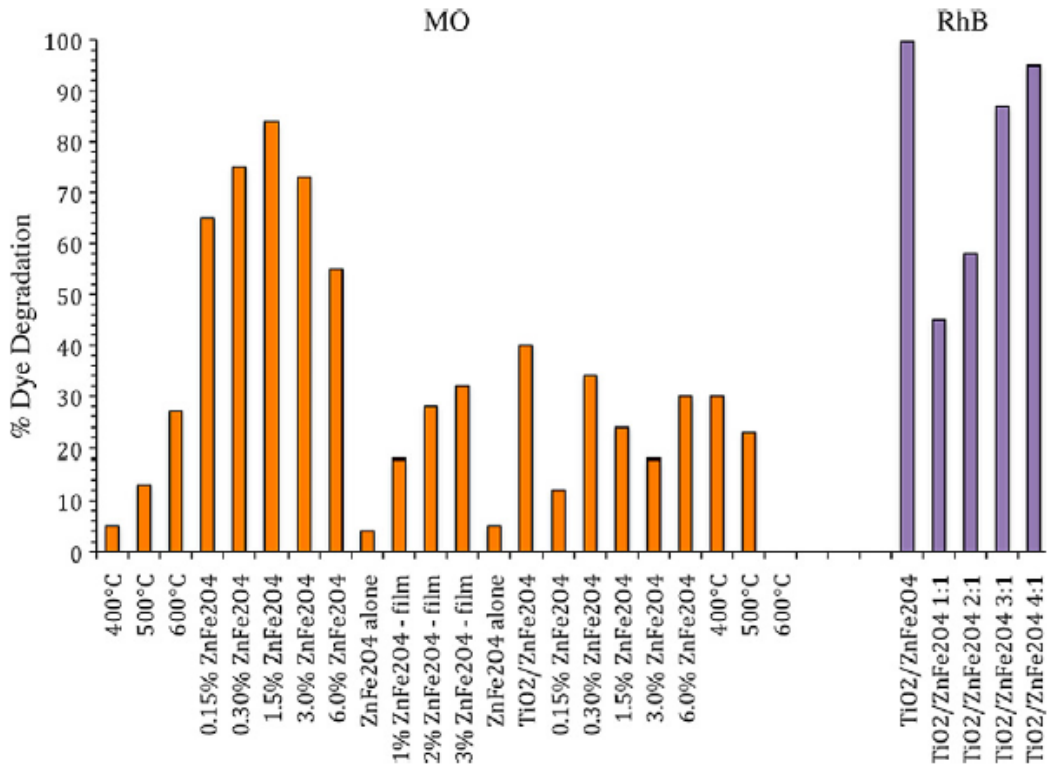

Figure 2-6: Degradation of MO and RhB dyes by $TiO_2/ZnFe_2O_4$ composite photocatalysts (Casbeer et al., 2012)

Table 2-5: reaction of various dye with ferrites and H_2O_2 with no applied irradiation (Casbeer et al., 2012)

Dye	Photocatalyst (+H_2O_2)	Dye (mg/L)	Catalyst loading (g/L)	Reaction time (h)	Degradation (%)
Bromophenol blue	$CoFe_2O_4$	50	25	24	2
	$CuFe_2O_4$	50	25	24	48
	$MnFe_2O_4$	50	25	24	0
Chicago sky blue	$CoFe_2O_4$	50	25	24	93
	$CuFe_2O_4$	50	25	24	95
	$MnFe_2O_4$	50	25	24	91
Eosin yellow	$CoFe_2O_4$	50	25	24	25
	$CuFe_2O_4$	50	25	24	53

	$MnFe_2O_4$	50	25	24	12
Phenol red	$CoFe_2O_4$	50	25	24	85
	$CuFe_2O_4$	50	25	24	86
	$MnFe_2O_4$	50	25	24	63
Reactive orange 16	$CoFe_2O_4$	50	25	24	21
	$CuFe_2O_4$	50	25	24	86
	$MnFe_2O_4$	50	25	24	6
Evans blue	$CoFe_2O_4$	50	25	24	73
	$CuFe_2O_4$	50	25	24	92
	$MnFe_2O_4$	50	25	24	8

CHAPTER 3

3 METHODOLOGY

3.1 Introduction

This chapter presents the preparation method for the $CuFe_2O_4$ photocatalyst as well as the description of photocatalyst characterization technique. The characterization techniques include nitrogen physisorption for BET specific surface area and pore size distribution, X-ray diffraction (XRD) for crystalline structure scanning and Field Emission Scanning Electron Microscopy (FESEM) for surface morphology capturing. In addition, the discussion about the operational procedures for the photo-degradation of methylene blue and glycerol solution as well as sample analysis is also presented in this chapter.

3.2 Chemicals

Table 3-1 shows the chemicals employed in the catalyst preparation, photocatalytic reaction and photocatalyst characterization. These chemicals were purchased from Sigma-Aldrich. The distilled water was readily available from the water purification system available in the laboratory of Universiti Malaysia Pahang (UMP).

Table 3-1 : List of chemicals and its applications

Chemical	Purity	Application
Copper (II) nitrate, $Cu(NO_3)_2$	99%	Catalyst synthesis
Iron (III) nitrate, $Fe(NO_3)_3$	99%	Catalyst synthesis
Sodium hydroxide, NaOH	10%	Catalyst synthesis
Glycerol	99%	Photocatalytic reactant
Methylene blue , $C_{16}H_{18}N_3SCl$	99%	Photocatalytic reactant
Hydrogen peroxide, H_2O_2	30%	Oxidizing agent
N_2/He mixture	N_2=30.03%, He=balance	BET analysis
He	>99.996%	BET analysis

N_2	>99.99%	BET analysis
Acetonitrile	99%	HPLC analysis

3.3 Photocatalyst preparation

There are several preparation methods to produce $CuFe_2O_4$ such as solid state reaction, co-precipitation, sol–gel process and combustion synthesis. The method employed in the current work was co-precipitation.

A total of 0.01 mol of $Cu(NO_3)_2 \cdot 3H_2O$ and 0.02 mol $Fe(NO_3)_3 \cdot 9H_2O$ were dissolved in 100 mL of distilled water. Under vigorous magnetic-stirring, the pH of the mixture was slowly raised by adding 10% NaOH solution to achieve pH of 10 followed by continuous stirring for 30 min. Subsequently, the suspension was heated to 95–100 °C for 2 h. After cooling, the prepared CF nanoparticle was transferred onto filter paper and then repeatedly washed with distilled water. The washed solid was remained on the filter paper and dried at 50 °C for 5 h and at 110 ^{0}C for 3 h. The dried material was ground and then calcinated at 600 °C for 1 h (Mahmoodi, 2011).

3.4 Photocatalyst Characterization

Catalyst characterization provides useful information on the physicochemical properties of the catalyst itself. The information from various characterization techniques is able to improve the understanding of the physicochemical attribution in relation to the photocatalytic performance. The catalyst prepared was characterized by the methods listed in Table 3-2.

Table 3-2 : List of catalyst characterization techniques and its equipment

Techniques	Equipment
N_2 Physisorption	Thermo-Scientific Surfer
Gas pycnometer	Pycnometer type 1305 Micromeritcs
XRD	Rigaku Miniflex II
FESEM	JEOL JSM-7800F

Subsequently, the following subsection will describe the fundamental theory and concept of these characterization techniques used in this work.

3.4.1 Nitrogen physisorption (BET)

Brunauer-Emmett-Teller (BET), is the most widely used procedure, which is an extension of the Langmuir's pioneer work. This instrument of model Thermo-Scientific Surfer was used to determine the specific surface area of the catalyst sample. The specific surface area of a powder was determined by physical adsorption of a gas on the surface of the solid by calculating the amount of adsorbate gas corresponding to a monomolecular layer on the surface. Physical adsorption results from relatively weak forces which is Van der Waals forces between the adsorbate gas molecules and the adsorbent surface area of the test powder. The most commonly used adsorbate is N_2 with the cross sectional area of 16.2 $Å^2$. The adsorption of N_2 is carried was carried out at the boiling point of nitrogen which is about 77.4K.The determination method was operated at the temperature of the liquid nitrogen. The amount of gas adsorbed can be measured by volumetric or continuous flow procedure. According to Braunauer, Emmet, & Teller (1938), BET adsorption isotherm is shown as :

$$\frac{1}{\left[V_a\left(\frac{P_o}{P}-1\right)\right]} = \frac{C-1}{V_m C} \text{x} \frac{P}{P_o} + \frac{1}{V_m C} \qquad (3\text{-}1)$$

where

P = partial vapour pressure of adsorbate gas in equilibrium with the surface at 77.4 K, in Pa

Po = saturated pressure of adsorbate gas, in Pa

V_a = volume of gas adsorbed at standard temperature and pressure (STP) (273.15 K and atmospheric pressure = 1.013 x 10^5 Pa), in millilitres

V_m = volume of gas adsorbed at STP to produce an apparent monolayer on the sample surface, in millilitres

C = dimensionless constant that is related to the enthalpy of adsorption of the adsorbed gas on the powder sample

The value of V_a was measured at each of not less than three values of P/Po. Then the BET value was plotted against P/Po following to equation (3-1). This plot usually yield a straight line in the approximate relative pressure range 0.05 to 0.3. The data was considered acceptable provided that the correlation coefficient, r, of the linear regression was not less than 0.9975; that is r^2 is not less than 0.995. From the resulting linear plot, we can obtain:

$$\text{slope} = \frac{C-1}{V_m\, C} \qquad (3\text{-}2)$$

$$\text{Intercept} = \frac{1}{V_m C} \qquad (3\text{-}3)$$

$$C = \left(\frac{\text{Slope}}{\text{Interceot}}\right) + 1 \qquad (3\text{-}4)$$

Then from the value of V_m determined, the specific surface area, S, can be calculated by the equation:

$$S = \frac{V_m\, N_a}{m \text{ x } 22400} \qquad (3\text{-}5)$$

Where

N = Avogadro constant (6.022×10^{23} mol^{-1})

a= effective cross-sectional area of one adsorbate molecule, in square metres (0.162 nm^2 for nitrogen and 0.195 nm^2 for krypton)

m= mass of solid catalyst, in grams

22400 = volume occupied by 1 mole of the adsorbate gas at STP allowing for minor departures from ideal, in millimetres.

An understanding of porosity of a solid material can be obtained by the construction of an adsorption isotherm by measuring the quantity of adsorbate on the surface over a wide range of relative pressures at constant temperature (Sing et al., 1985). The adsorption isotherm is obtained point-by-point by admitting successive known volumes of N_2 to the adsorbent (solid surface) and measuring the equilibrium pressure. Similarly, desorption isotherm can be obtained by measuring the quantities of gas removed from the sample as the relative pressure is lowered. The volume of nitrogen adsorbed (V_{ads}) can be converted to the volume of N_2 (V_{liq}) contained in the pores using

$$V_{liq} = \frac{P_a V_{ads} V_m}{RT} \qquad (3\text{-}6)$$

Where

Pa = Ambient pressure

T = Ambient temperature

Vm = molar volume of the liquid N_2 (34.7 $cm^3.mol^{-1}$)

The total pore volume was derived from the amount of vapour adsorbed at a relative pressure close to unity, by assuming that the pores are then filled with liquid N_2. The isotherm will remain nearly horizontal over a range of P/Po near the unity if the solid material contains no macropores (pores width > 50nm). Then this pore volume was well defined. The isotherm rose rapidly near P/Po close to 1 for macropores. Therefore, the limiting adsorption may be identified with the total pore volume.

Thermo-Scientific Surfer offers the capability of using either branch of the isotherm for the pore size distribution calculation. Mesopore size calculations were executed by assuming cylindrical pore geometry using the Kelvin equation (Sing, et al., 1985):

$$r_k = \frac{-2V_m \gamma}{RT\ln(\frac{P}{Po})} \qquad (3\text{-}7)$$

Where

Υ = the surface tension of N_2 at its boiling point (8.85 $ergs.cm^2$ at 77.4 K)

V_m = the molar volume of liquid N_2 (34.7 cm^3/mol)

R = gas constant (8.314 E^7 egrs/K.mol)

T = N_2 boiling point (77.4 K)

P/Po = relative pressure of N_2

r_k = the kelvin radius of the pore

By using the appropriate constants for N_2, equation (3-7) can reduce to:

$$r_k = \frac{4.15}{\log(\frac{P}{Po})} \qquad (3\text{-}8)$$

The kelvin radius is the radius of the pore in which condensation happens at P/Po. However, r_k does not represent the actual pore radius as some adsorption had happened prior to condensation on the walls of the pore. Moreover, an adsorbed layer remained on the walls when evaporation take place during desorption.

Hence, the actual pore radius (r_p) is given by:

$$r_p = r_k + t \qquad (3\text{-}9)$$

Where t is the thickness of the adsorbed layer. The t-value was estimated by:

$$t = \left[\frac{13.99}{\log\left(\frac{P}{Po}\right)+0.034}\right]^{1/2} \qquad (3\text{-}10)$$

3.4.2 Field Emission Scanning Electron Microscopy (FESEM)

A FESEM is microscope that works with electrons instead of light. These electrons are liberated by a field emission source. The object is scanned by electrons according to a zig-zag pattern.

FESEM is used to reveals information such as sample morphology or texture, sample topography, sample compositions, crystalline structure and orientation of materials which contribute to the structure of the catalyst from electron–sample interactions by directing a beam of high energy electrons to produce a variety of electrons emitted from surface of the catalyst with instrument JEOL JSM-7800F using the accelerating voltage of 5 kV.

A detector caught the secondary electrons and an image of sample surface was constructed by comparing the intensity of these secondary electrons to the scanning primary electron beam. Finally the image was displayed on a monitor. Commonly, data can be collected from a selected area of the surface of the specimen and a three dimensional image was obtained. During the acceleration of electrons in FESEM, the electrons carried a significant amount of kinetics energy generated by electrons-sample interactions which consequently dissipated as signals. These signals included secondary electrons which produced the FESEM images (morphology and topography of samples), backscattered electrons (BSE) and diffracted backscattered electrons (Michler, 2004). The dissimilarities of the image are due to difference in electron collection efficiency that depends on the angle of emission and atomic number of elements. Energy dispersive usually comes with field emission scanning microscopy analysis (FESEM) for better analysis results.

3.4.3 X-ray Diffraction (XRD)

XRD measurements was carried out on a Rigaku Miniflex II. XRD is a non-destructive analytical technique which is widely used for the identification of structure, crystalline phases, and also sizes of crystallites of natural or synthetic materials. The specimen was initially ground to fine powder (<100 μm). It was then placed on a glass specimen holder and pressed using a glass slide. Scanning of sample was then performed starting from 3˚ to 80˚ at a speed of 1˚/min. Peaks obtained from the analysis were evaluated using The International Centre for Diffraction Data (ICDD) database search match interpretation method to determine the type of phases present. The schematic of X-ray Diffusion is presented in Figure 3-1.

XRD was based on the constructive interference of monochromatic X-rays and a crystalline sample. The X-rays were generated by a cathode ray tube, filtered to produce monochromatic radiation, collimated to concentrate and directed towards the sample. The interaction of the incident rays with the sample produced constructive interference when conditions fulfil Bragg's Law as in the equation below (Barbara & Christine, 2012):

$$n\lambda = 2d\sin\theta \qquad (3\text{-}11)$$

Where

n = the order of reflection (integer)

λ = wavelength of x-ray beam (nm)

d = inter plane distance of crystal (d-spacing)

θ = angle of incidence (degree)

This law relates the wavelength of electromagnetic radiation to the diffraction angle and the lattice spacing in a crystalline sample. These diffracted X-rays were then detected, processed and counted. By scanning the sample through a range of 2θ angles, all possible diffraction directions of the lattice were attained due to the random orientation of the powdered material. The mean crystalline size can be obtained by the Scherrer equation:

$$D = \frac{k_{Sch}\lambda}{\beta_d cos\theta} \qquad (3\text{-}12)$$

Where

D = crystalline size (Å)

k_{Sch} = Scherrer constant

β_d = angular width of half-maximum intensity (degree)

λ = X-ray wavelength

θ = Bragg's angle (degree)

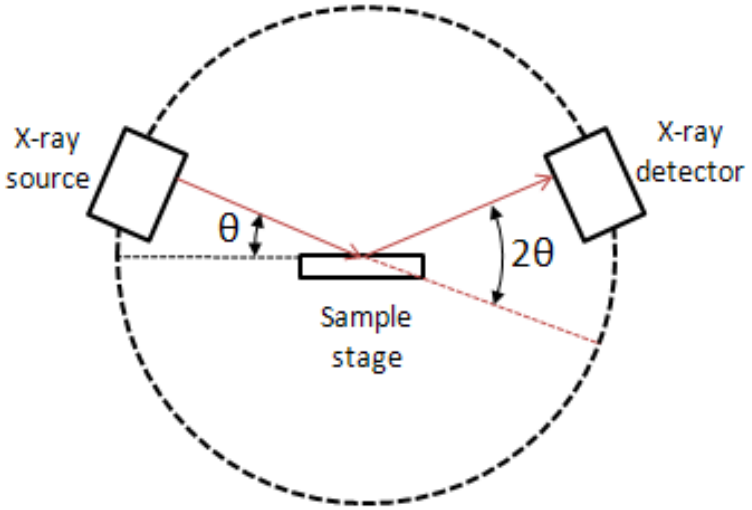

Figure 3-1: Schematic diagram of XRD

3.4.4 Gas pycnometer

In this work, constant volume helium gas displacement Pycnometer type 1305 Micromeritics which is shown in Figure 3-2 was used to measure the volume and density of catalyst. Gas pycnometer can measure the volume and density in powder, porous and irregularly shaped solids form and can be obtained rapidly as well as accurately. The air was employed for inert low-surface materials on which negligible adsorption of gas occurs; while helium was employed for the fine powders or porous materials and the activated samples with high surface area.

A constant volume gas pycnometer was composed of a sample chamber with a screw cap, a tank and an absolute pressure transducer. The most vital part of the pycnometer is the pressure detector. It consists of a metal bellows and a signal light. The signal light indicates when the bellows is at its final position. The bellows was provided with stops in both directions so that evacuation or moderate overpressuring will not damage it. The pressure in the bellows can be set, however pressures between 400 and 500 mm Hg were found to give the most optimum results. The chamber and tank were connected pneumatically through a tube with coupling valve. The tank also connected to the pressure transducer so that the helium gas supply through the tube with a main coupling valve. The catalyst powder was put inside the chamber and weighted, then inserted into the gas

pycnometer to analyse the volume and the density. The test was set as three circles in order to obtain a more accurate result.

There are few theories of the operation of gas pycnometer. The gas in the system expands from the initial volume *V1* to a volume of *V2* when the gas pressure in the pycnometer system is reduced from an initial pressure P1 to a final pressure P2. Next, the initial gas volume is reduced to *V1s* when a sample of volume *Vs* is placed in the system and thereby the pressure is reduced form P1 to P2. Therefore, the volume of the gas expand from V1s to V2s. At constant temperature and relatively low pressure, the perfect gas law is fulfilled and the change in volume ΔVs due to the presence of the sample volume *Vs* is

$$V_s = \frac{(P_1 - P_2)}{P_2} \times V_s \qquad (3\text{-}13)$$

Experimentally, it is easier to get Vs by a volume parameter σ. Vs, can be calculated from a measurement of ΔVs provided that the initial pressure P1 and the final pressure P2 are known. The volume parameter can be expressed as:

$$\sigma = \frac{V_s}{\Delta M} = \frac{P2}{P1 - P2}\frac{\Delta V_s}{\Delta M} \qquad (3\text{-}14)$$

Where

ΔM = difference between the final dial readings with and without a sample

σ = value determined by measuring an object of known volume such as a steel ball.

The volume of an unknown sample can be calculated simply by the equation (3-15) once the value of σ is obtained (Keng, 1969),

$$Vs = \sigma \Delta M \qquad (3\text{-}15)$$

Figure 3-2: Diagram of gas pycnometer

3.5 Photocatalytic-degradation of methylene blue

The photocatalytic reaction was carried out in a multi-ports quartz photoreactor. It comprised of two housings whereby a 500 mL flask with flat end was employed as methylene blue solution container whilst the smaller diameter housing would host a vertically-built Xenon lamp. The second housing acts as protection layer to avoid direct contact between the Xe-source and the methylene blue solution.

For the photocatalytic reaction, a total of 200 mL of 20 ppm methylene solution was used in each runs. Reaction was carried out under atmospheric pressure and room temperature. A total of 0.2g $CuFe_2O_4$ photocatalyst was added into the methylene blue solution (Figure 3-3), yielding a catalyst loading of 1.0 $g.L^{-1}$. For experiment that was used to test the effectiveness of fenton system, the amount of H_2O_2 was varied. Then, the solution mixture was magnetic-stirred for 30 min to ensure homogeneity. Subsequently, the light-containing compartment was locked into the reactor flask. Before reaction commenced, 5 mL of sample was obtained using a dropper from the port locate at the side of the reactor flask, labelled R-0 (reactant at t=0 min). The visible light source was then be switched on as shown in Figure 3-4, and timer was started. 5 mL sample was obtained at every 60 minutes interval for 2 h, labelled R-60, R-120, R-180 and R-240, R-300 and R-360. While

for experiment with H_2O_2 added, the sample was obtained at every 20 minutes interval for 2 h. The collected samples in a centrifuge tube were kept in a dark place to prevent further photoreaction.

The samples collected in centrifuge tubes were centrifuged at 5800 rpm for 20 min to separate the catalyst from the reactant samples. Subsequently, each sample was carefully drawn out into a cuvette and was then examined using UV-Vis.

Figure 3-3 : Photoreactor with methylene blue solution and $CuFe_2O_4$

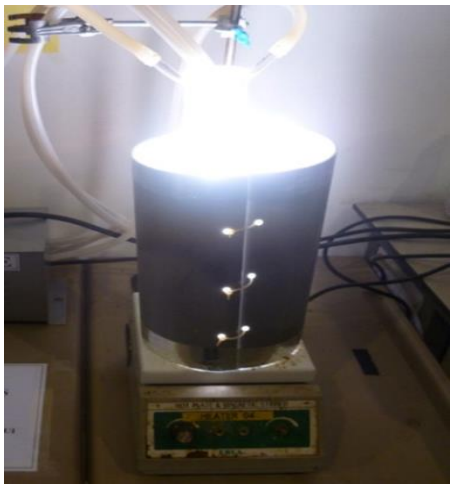

Figure 3-4 : Photoreactor with the light-containing compartment

3.6 Glycerol Photocatalytic-degradation

For the photocatalytic degradation of glycerol solution, the experimental procedure was similar to the methylene blue photocatalytic degreadation written in subtopic 3.5. However, the difference was that a total of 0.4 g $CuFe_2O_4$ photocatalyst was added into the 0.5 v/v% glycerol solution, yielding a catalyst loading of 2.0 gL^{-1}. 5 mL sample was obtained at every 60 minutes interval for 6 h instead of 2 h and for experiment with H_2O_2 added, the sample was obtained at every 15 minutes interval for 4 hours. Subsequently, each collected sample was carefully drawn out and filtered before inserted into vial before examined using HPLC. The area and height at the highest peak was recorded for each sample.

3.7 Sample analysis

The samples of experiment were analysed by using Ultraviolet-visible Spectroscopy (UV-VIS) and High Performance Liquid Chromatography (HPLC). Methylene blue samples were analysed by UV-VIS while glycerol samples were examined by HPLC. Table 3-3 showed the list of techniques and equipment for the sample analysis.

Table 3-3: List of techniques and equipment for sample analysis

Techniques	Equipment
UV-VIS	Hitachi U-1800 spectrophotometer
HPLC	Agilent 1200 Infinity Series

3.7.1 Ultraviolet-visible Spectroscopy (UV-Vis)

Methylene blue samples were analysed by using a Hitachi U-1800 spectrophotometer which is shown in Figure 3-5. The instrument measures the absorption spectrum of a sample at wavelengths in the range 190 to 900 nm. The light source used are deuterium lamp at wavelength in the range 190-350 nm (UV region) and halogen (W1) lamp at wavelength in the range 340-2500 nm (VIS/NIR region).

Figure 3-5: Hitachi U-1800 spectrophotometer

UV-Vis utilizes light to determine the absorbance or transmission of a chemical species in either solid or aqueous state. The light from the light source either a visible or UV light is converged and enters the monochromator which is shown in Figure 3-6 (Black colour). It is separated into its component wavelengths by a prism or diffraction grating. A half mirrored device is used to split the monochromatic (single wavelength) beam into two equal intensity beams. The sample beam (coloured red), passes through a small transparent cuvette containing the solution of the methylene blue that is being tested with copper ferrite catalyst and being studied in a transparent solvent. The other beam, the

reference (coloured green), passes through an identical cuvette containing only the solvent in which pure water is used. Electronic detectors are used to measure the intensities of these light beams and compared. The intensity of the reference beam, is defined as I_0, which should have suffered little or no light absorption. The intensity of the sample beam is defined as I. Then, the spectrometer automatically scanned all the component wavelengths in the manner described. The ultraviolet (UV) region scanned is normally from 200 to 400 nm, and the visible portion is from 400 to 800 nm.

If the sample analysis does not absorb light of a given wavelength, $I = I_0$. On the contrary, if the sample analysis absorbs light then I is less than I_0. This difference was plotted on a graph versus wavelength, as shown in the example of figure 10. Absorption may be represented as transmittance ($T = I/I_0$) or absorbance ($A = \log I_0/I$). If no absorption has taken place, T = 1.0 and $A = 0$. Most spectrometers show absorbance on the vertical axis, and the normally observed range is from 0 (100% transmittance) to 2 (1% transmittance). λ_{max} is the wavelength of maximum absorbance value.

Different compounds have very different absorbances or transmittance. Therefore, in order for the light energy to be received by the detector, absorbing compounds must be examined in dilute solution. The most generally used solvents are water, ethanol, hexane and cyclohexane. Solvents that have double or triple bonds, or heavy atoms (e.g. S, Br & I) are avoided. This is due to the absorbance of a sample will be proportional to its molar concentration in the sample cuvette, a corrected absorption value known as the molar absorptivity. Molar absorptivity is used when it is use to compare the spectra of different compounds. It is defined as:

Molar absorptivity, $\varepsilon = A/ c\ l$

Where

A = absorbance

C = sample concentration in moles/liter

l = length of light path through the cuvette in cm

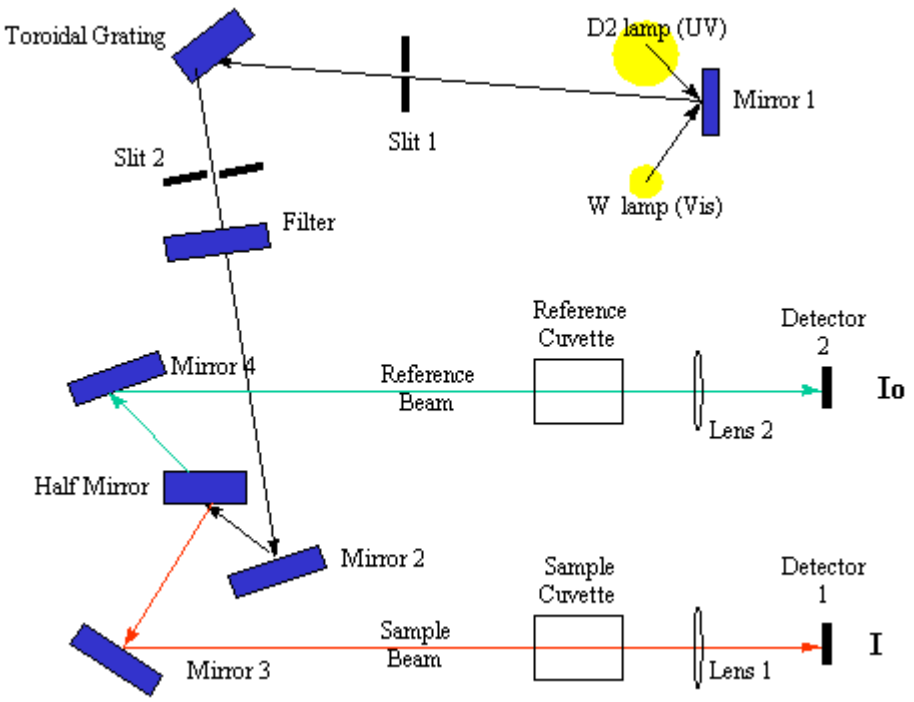

Figure 3-6 : The Jasco V-550 optical system schematic diagram

In this study, the samples of methylene blue were centrifuged at 5800rpm for 20 minutes in order to separate the methylene blue and $CuFe_2O_4$. The centrifuged sample was transferred carefully to UV-VIS cuvette by a dropper. Before the sample analysis started, a cuvette filled with distilled water was used as the baseline. After that, the sample cuvette filled with methylene blue was analysed and the example results from UV-VIS analysis is shown in Figure 3-7. The absorption at the highest peak was recorded. The peak for methylene blue was normally at wavelength in the range of 620-680nm.

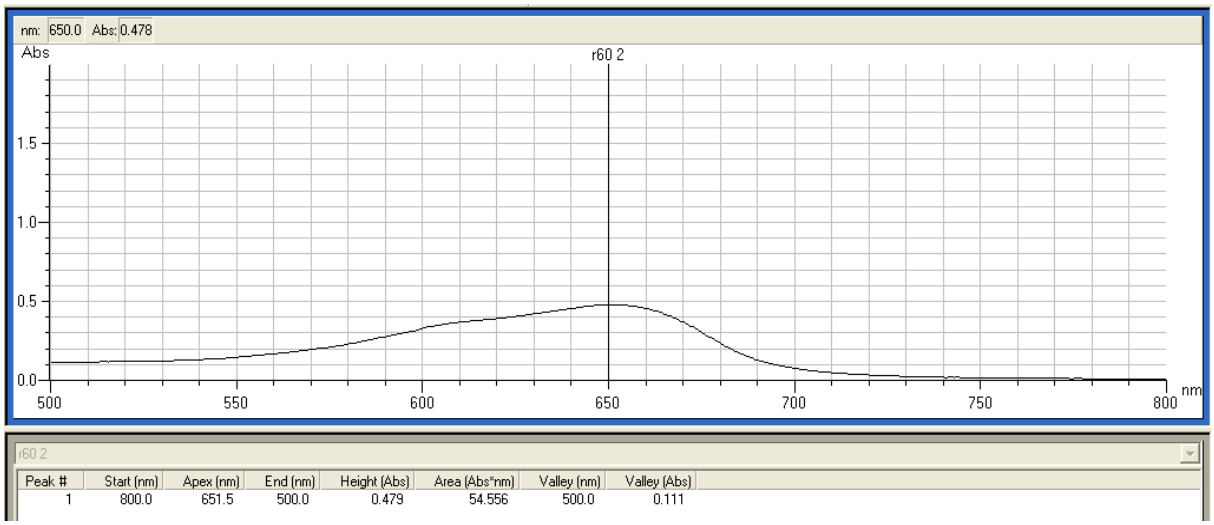

Figure 3-7: Example result from UV-VIS analysis

3.7.2 High Performance Liquid Chromatography (HPLC)

HPLC is extensively used in all aspects of analysis including assay, dissolution analysis, impurity profile, forced degradation studies, process control, and drug metabolism studies (Wang et al., 2014). A model of Agilent 1200 Infinity Series HPLC which is shown in Figure 3-10 was used in the analysis of photo-degradation of glycerol solution in this research work. HPLC is a separation technique that involves the injection of a small volume of liquid sample and into a tube packed with tiny particles (3 to 5 micron in diameter called the stationary phase). The individual components of the sample were moved down the column with a liquid (mobile phase) forced through the column by high pressure delivered by a pump. These components are separated from one another by the column packing that involves various chemical and physical interactions between their molecules as well as the packing particles. Then, these separated components were detected at the exit of this column by a flow-through device (detector) that measures their amount. Liquid chromatogram was the output from this detector.

In this study, glycerol standard solution was prepared in low concentration for the purpose of calibration. Mobile phase, acetonitrile (ACN) was prepared in the ratio of ACN: water is 70: 30. Next, filtration kits and vacuum pump system was assembled and the mobile phase was filtered by vacuum filtration unit. The flask containing filtrate was transferred

into ultrasonicator and sonification was performed for half an hour. The solvent was then poured carefully into solvent bottle that is connected to HPLC. For the sample preparation, the samples were centrifuged for 20 minutes and filtered. The filtered sample was injected into a vial for HPLC analysis. For the chromatographic analysis, flat baseline was ensure to obtain before the analysis was started. The flowrate of the mobile phase was set to 1 ml/min. The method was pressed and analysis was started. Finally, the retention time, height and area from liquid chromatogram (Figure 3-8) were recorded.

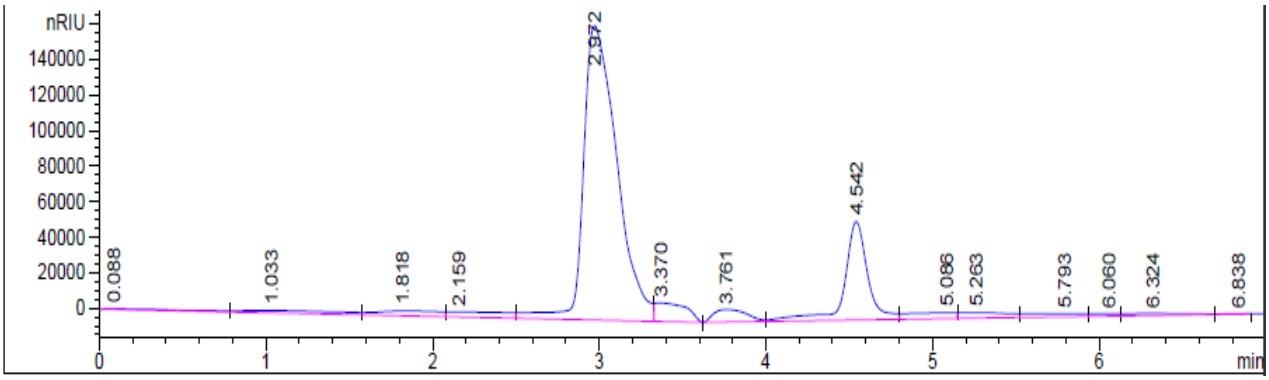

Figure 3-8: Liquid chromatogram

A chromatogram can be interpreted in two main ways which are determination of the peak height of a chromatographic peak as measured from the baseline and the determination of the peak area which can be shown in figure 3-9.

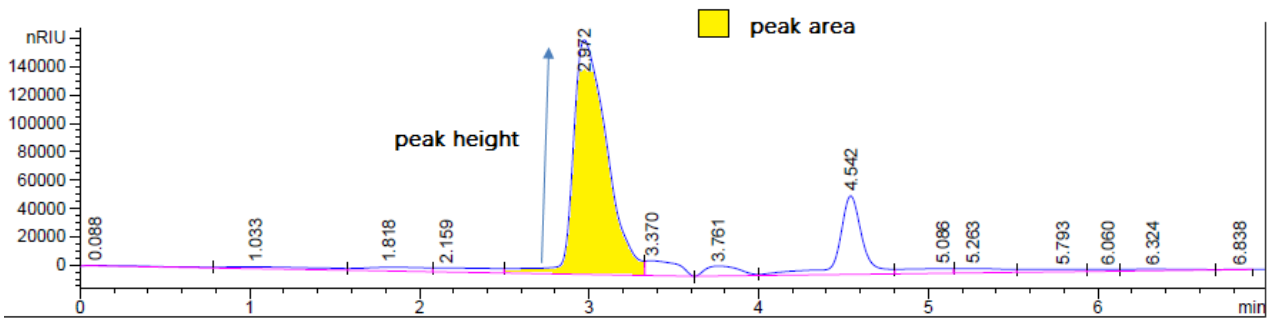

Figure 3-9: Determination of peak height and area

Figure 3-10: Agilent 1200 Infinity Series HPLC instrument

CHAPTER 4

4 RESULTS AND DISCUSSION

4.1 Introduction

In this chapter, physicochemical properties of the photocatalyst, $CuFe_2O_4$ were characterized via several well-established techniques including gas pycnometer, BET specific surface area and XRD. Subsequently, photocatalytic-degradation of methylene blue and glycerol solution were tested. This chapter also covers Langmuir-Hinshelwood modelling and correlations between the photocatalytic activity and the physicochemical properties.

4.2 Characterization of Photocatalyst

4.2.1 Nitrogen Physisorption (BET)

By using a Thermo Scientific Surfer surface analyser and Surface Acquisition software, the adsorption-desorption isotherms of N_2 adsorbate on calcinated $CuFe_2O_4$ was obtained. The isotherm is displayed in Figure 4-1. The characteristic features of the isotherm were its hysteresis loop, which was associated with capillary condensation taking place in mesopores, and the limiting uptake over a range of high P/P_o. P/P_o in this isotherm was 0.95. The initial part of the isotherm was attributed to monolayer-multilayer adsorption with the given adsorptive on the same surface area of the adsorbent in a non-porous form (Sing et al., 1985).

The specific surface area of calcinated $CuFe_2O_4$ photocatalyst was calculated from the N_2 adsorption data according to the Brunauer-Emmet-Teller (BET) method using relative pressure (P/P_o) values. The pore volume (Gurvich) at $P/P_o = 0.95$ was determined to be 0.17 cm^3 /g. The specific surface area of $CuFe_2O_4$ was determined using 2 Parameters Line as shown in Figure 4-2. The surface was evaluated and found to be 102.37 cm^2 /g. The BJH cumulative pore volume was obtained which was 0.1866 cm^3/g. These results were summarises in Table 4-1.

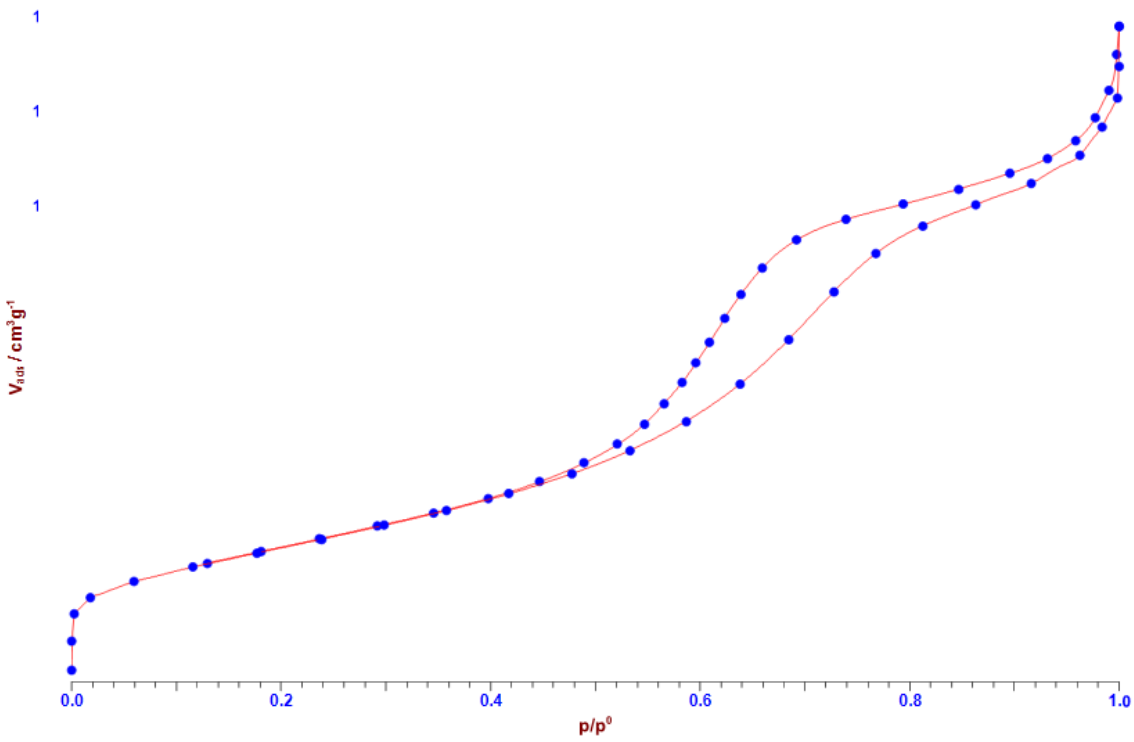

Figure 4-1: Adsorption-desorption isotherm of $CuFe_2O_4$ using N_2 as adsorbate

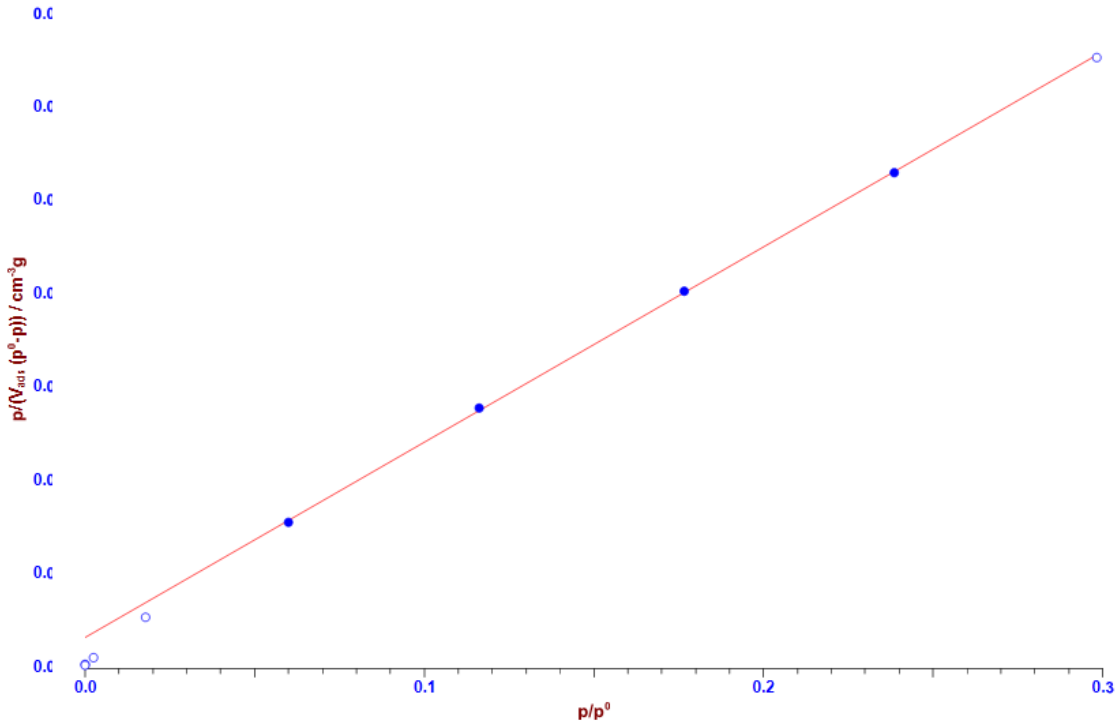

Figure 4-2: Surface area (BET) 2 Parameters Line

Table 4-1: Information of nitrogen physisorption analysis

Total Pore Volume (cm^3/g)	0.17
Pore Diameter (Å)	52.67
Cumulative volume of pore (cm^3/g)	0.19

4.2.2 XRD Diffraction Pattern

The synthesized $CuFe_2O_4$ was subjected to crystallinity characterization with XRD. XRD is a non-destructive analytical technique which is widely used for the identification of structure, crystalline phases as well as sizes of crystalline of natural or synthetic materials.

The whole set results of XRD pattern that obtained from 2θ =3° to 80° is shown in Figure 4-3. The value of 2θ, size and phase name are tabulated in Table 4-2. The crystal size of the prepared photocatalyst was found to be in the range of 4 to 150 nm. The 2θ values at 18.56°, 30.08°, 34.82°, 36.03°, 37.27°, 54.23° and 62.25° can be attributed to (101), (112), (103), (211), (202), (312) and (224) planes, respectively. The position and relative intensities of all peaks shown in the XRD pattern conform well to the XRD pattern of $CuFe_2O_4$ synthesized by Ghahremanzadeh et al. (2014). It indicated that the synthesized $CuFe_2O_4$ with the plane at (101), (112), (103), (211), (202) and (224) depicted face-centred cubic $CuFe_2O_4$. The current result also revealed the presence of spinel structure of $CuFe_2O_4$. The diffraction peaks of these samples analysis are narrow and strong, indicative of good crystallinity (Uddin et al., 2014).

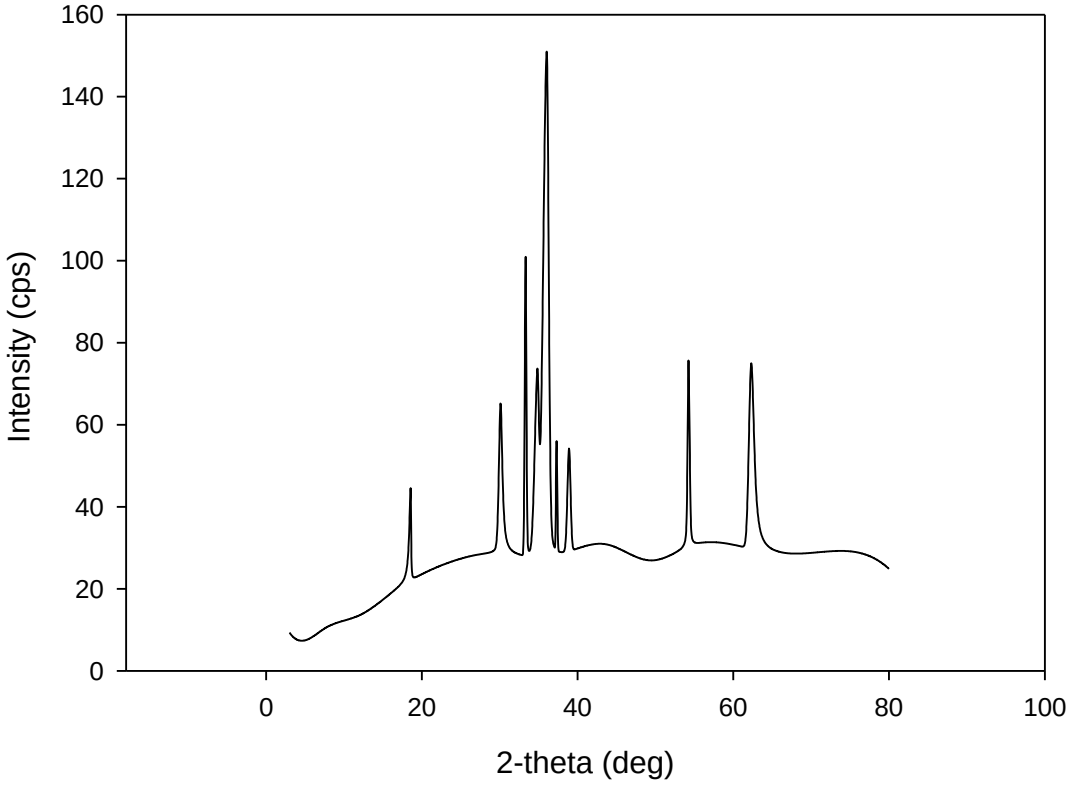

Figure 4-3: XRD pattern of $CuFe_2O_4$

Table 4-2: the value of 2-theta, size and phase name of synthesized $CuFe_2O_4$

2-theta (deg)	Size (nm)	Phase name
18.56	88	Copper ferrite (101)
30.082	14	Copper ferrite (112)
34.82	11	Copper ferrite (103)
36.03	4	Copper ferrite (211)
37.27	148	Copper ferrite (202)
54.23	100	Copper ferrite (312)
62.25	9	Copper ferrite (224)

4.2.3 FESEM Analysis

FESEM is one of the most versatile and well known analytical technique. It is used to visualize very small topographic details on the surface or entire or fractioned objects.

In this study, the morphology of the photocatalyst which was calcined at 600°C by co-precipitation method were observed by FESEM as shown in Figures 4-4 and 4-5. From

the analysis, it showed the homogeneity and uniformity of particle sizes. The $CuFe_2O_4$ particles were branched structures with rod shapes. The size was much less than 1 µm. This FESEM also confirms the $CuFe_2O_4$ particle sizes are made up of nanomaterials.

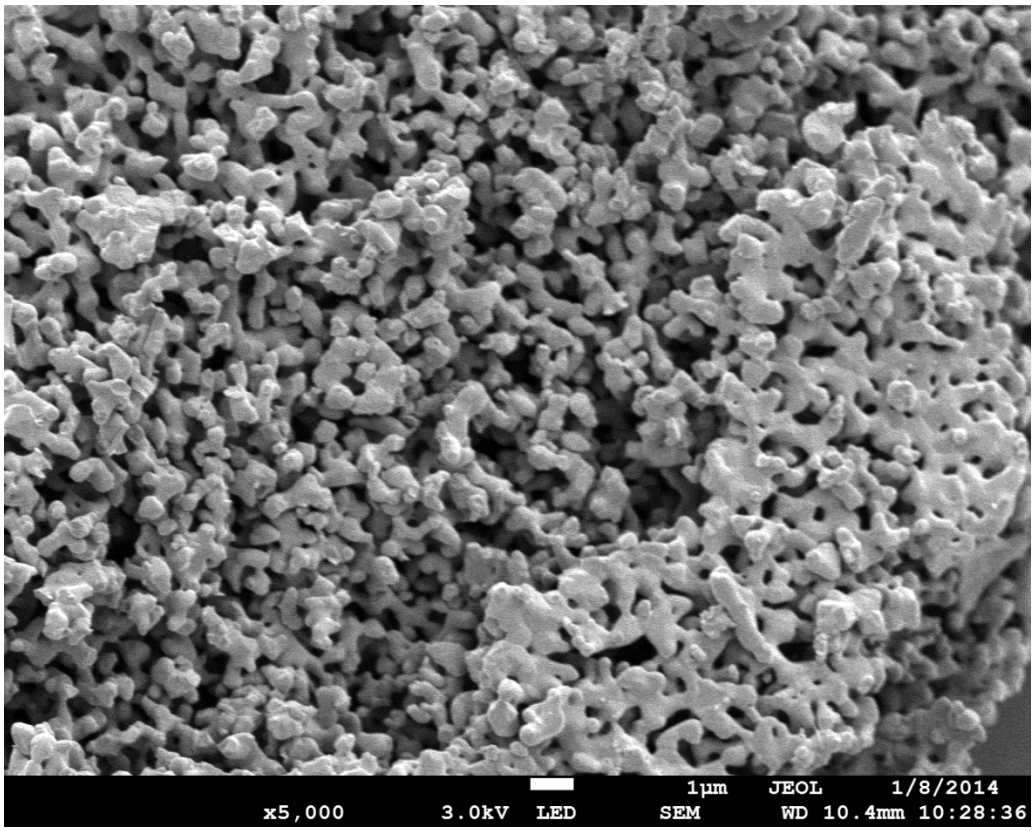

Figure 4-4: FESEM micrograph of $CuFe_2O_4$ after calcined at 600°C at 5,000X

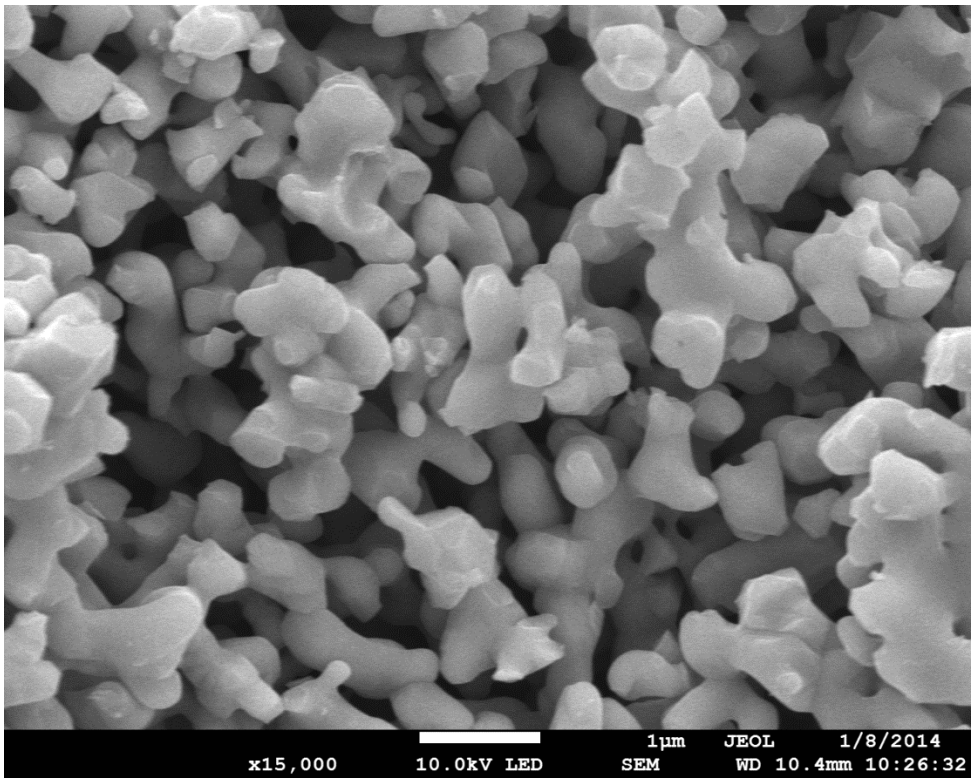

Figure 4-5: FESEM analysis of $CuFe_2O_4$ at 15,000X

4.2.4 Density of Photocatalyst

The density of synthesized photocatalyst was analysed from gas pycnometer unit which is Pycnometer type 1305 Micrommeritics. The result was repeated for three cycles to increase the accuracy. An average value of the three results was taken as the final density of the photocatalyst. The measurements from pycnometer was tabulated in Table 4-3 and graph of density versus cycle number can be observed in Figure 4-6.

Table 4-3: Density of copper ferrite

Cycle	Volume (cm^3)	Density (g/cm^3)
1	0.1634	2.4928
2	0.1631	2.4979
3	0.1632	2.4953

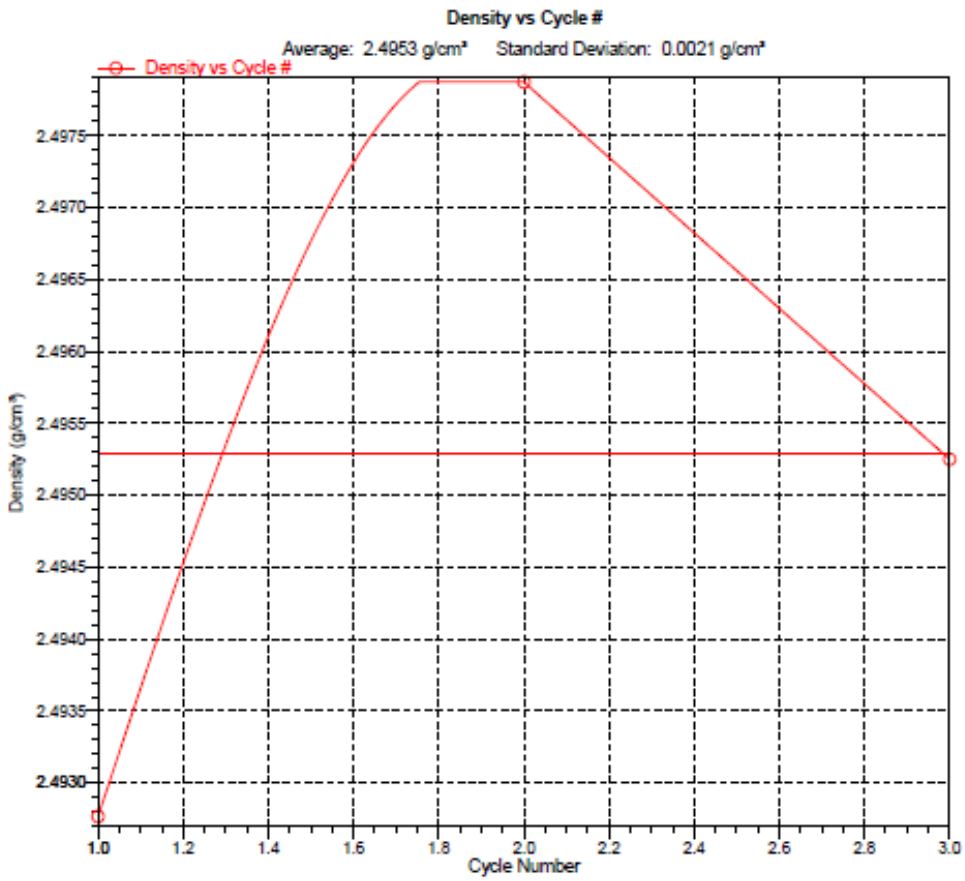

Figure 4-6: Graph of density versus cycle number of $CuFe_2O_4$

From Table 4-3, the density of photocatalyst, $CuFe_2O_4$ from the three average value was 2.50 g/cm^3. According to Ahmed et al (2009), the result of $CuFe_2O_4$ indicated that it possessed the bulk density of 3.93 g/cm^3 with a calcination temperature of 1100°C. However, the results obtained from gas pycnometer did not exhibit same result, probably due to the different synthesis method as well as calcination temperature (600°C) employed to produce the photocatalyst. Consequently, this may have result in different porosity; hence the density.

4.3 Photoreaction Study

4.3.1 Photocatalytic-degradation of Methylene Blue

Figures 4-7 and 4-8 showed the influence of photocatalyst loading of 0.5 g/L and 1.0 g/L in methylene blue solution under visible light source irradiation. Each graph displayed the degradation of methylene blue as a function of time. It indicated that by using $CuFe_2O_4$ as photocatalyst in the reaction, a considerable amount of methylene blue was degraded. In other words, this implied that $CuFe_2O_4$ is an effective photocatalyst towards photo-degradation of methylene blue under visible light irradiation. It can be seen that, the photo-degradation of methylene blue is relatively effective with the increasing loading of photocatalyst. This is due to the availability of active sites on $CuFe_2O_4$ particles surface. As the photocatalyst loading increased, the corresponding available active sites also increased. Moreover, the visible light energy that would be absorbed by $CuFe_2O_4$ is expected to increase accordingly at a higher loading of photocatalyst. It is believed that the availability of active site on $CuFe_2O_4$ particles surface and the light penetration of photoactivating light into the reactor are vital to the photocatalytic degradation of methylene blue solution. The proposed photocatalysis mechanism of $CuFe_2O_4$ is as follow (Valizadeh et al., 2014; Casbeer et al.,2012):

$$CuFe_2O_4 + hv \rightarrow CuFe_2O_4\ (e^-_{cb} + h^+_{vb}) \quad (4\text{-}1)$$

$$CuFe_2O_4\ (e^-_{cb} + h^+_{vb}) \rightarrow CuFe_2O_4 + heat \quad (4\text{-}2)$$

$$CuFe_2O_4 + H_2O_{ads} \rightarrow CuFe_2O_4 + OH^- + H^+ \quad (4\text{-}3)$$

$$e^-_{cb} + O^{2ads} \rightarrow O^{2-} \quad (4\text{-}4)$$

$$h^+_{vb} + OH^- \rightarrow \cdot OH \quad (4\text{-}5)$$

$$\cdot OH + MB \rightarrow H_2O + CO_2 \quad (4\text{-}6)$$

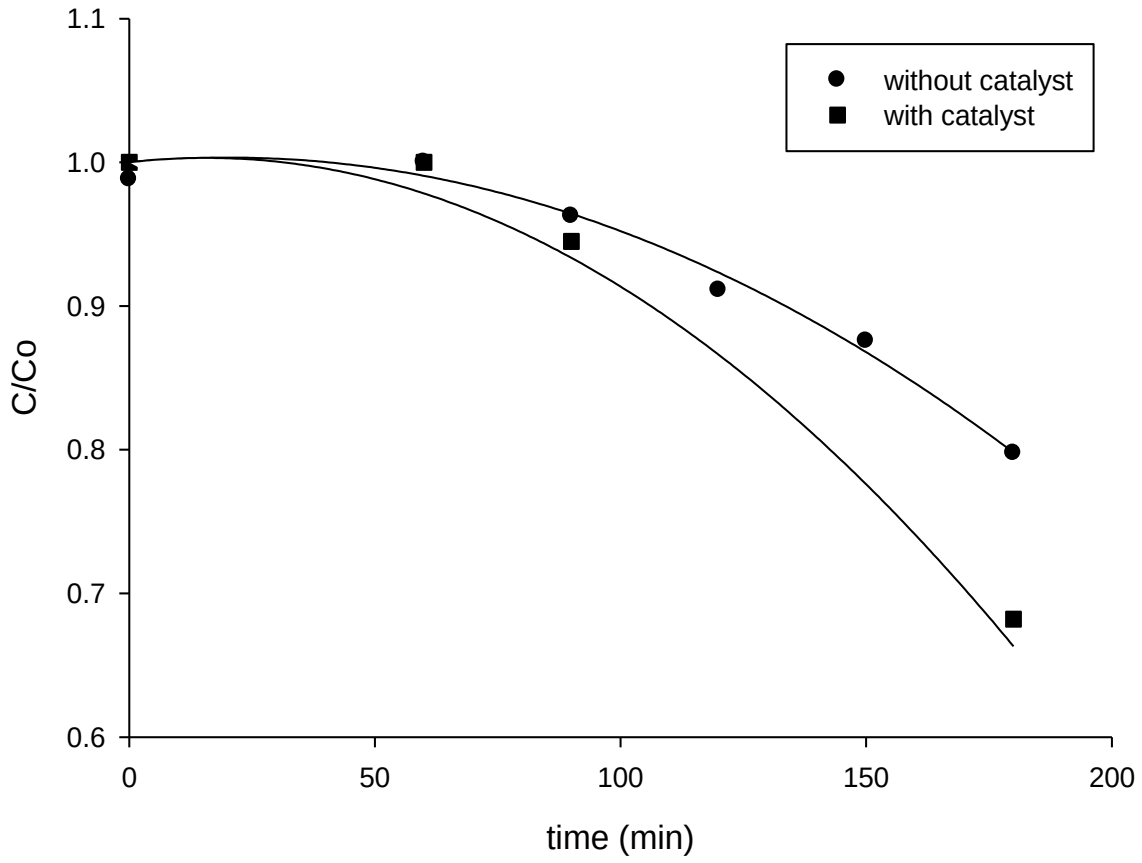

Figure 4-7: Photo-degradation of 20 ppm methylene blue with 0.5 g/L $CuFe_2O$

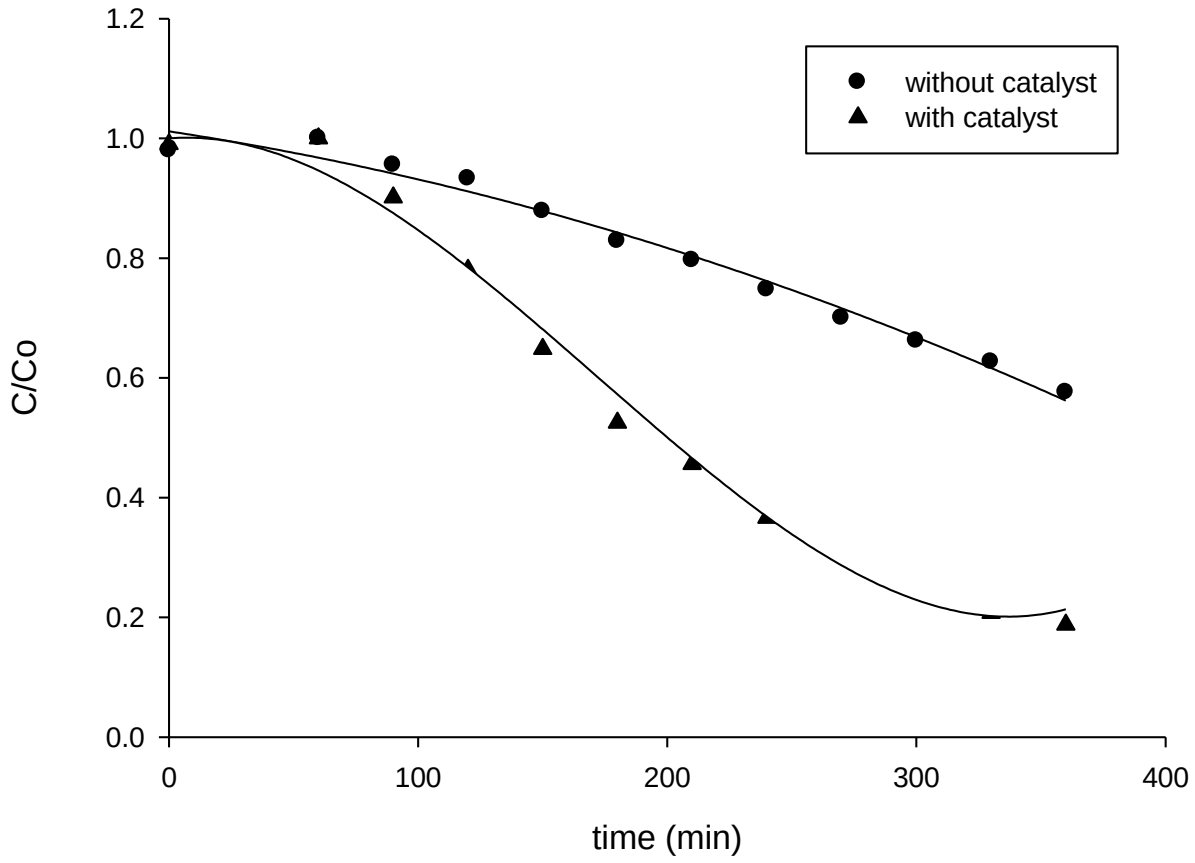

Figure 4-8: Photo-degradation of 20 ppm methylene blue with 1.0 g/L $CuFe_2O$

Figure 4-9 shows the colour changes of methylene blue from higher concentration to lower concentration. This has indicated that there was photocatalytic activity exhibited by the $CuFe_2O_4$ in the current work.

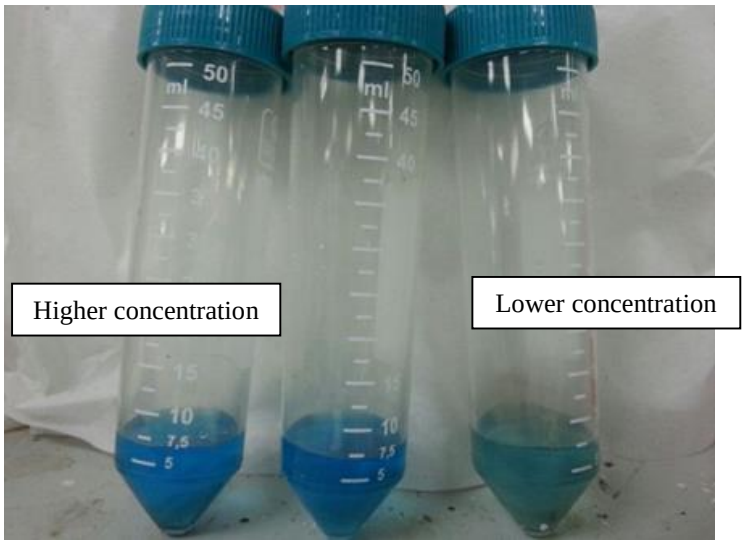

Figure 4-9 : Photo-degradation of methylene blue solution

The conversion of methylene blue photo-degradation was calculated by using Equation (4-7) and is tabulated in Table 4-4:

$$\text{Degradation conversion}, X(\%) = \frac{C_{AO} - C_A}{C_{AO}} \times 100 \qquad (4\text{-}7)$$

Table 4-4: Conversion of methylene blue photo-degradation

Catalyst loading (g/L)	Conversion, X (%)
0.5	19.28
1.0	41.26

However, an excess of photocatalysts may impede further penetration of incident light into the reactor. Although the concentration of photocatalsyt increase as well as the available avtive site, but the light penetration and the consequent photoactivated volume of the reaction shrink. The penetration of light is cloaked in the reactor by the large amount of the photocatalyst in the reaction mixture and thus blocking the light source irradiation. As the inner photocatalyst cannot absorbed the light energy and resulted the failure in generation of ·OH even though the light absorption of the outer photocatalyst increases. As a result, the photo-degradation of methylene blue will be decreased. It can be indicated that when the photocatalyst loading is below its optimum value, the available active site on the photocatalyst particles surface increases with the increasing photocatalyst loading. However, on the contrary, the photocatalyst loading has to be optimized when it is above its optimum value.

On top of that, another reason for the decreasing photocatalytic activity at extremely high concentration of photocatalyst loading is due to the activated $CuFe_2O_4$ can be deactivated by the collision with ground state $CuFe_2O_4$ molecules. The deactivation can be justified by the following equation below:

$$CuFe_2O_4^{\#} + CuFe_2O_4 \rightarrow CuFe_2O_4^{*} + CuFe_2O_4 \qquad (4\text{-}8)$$

Where

$CuFe_2O_4^{\#}$ = photoexcited $CuFe_2O_4$

$CuFe_2O_4^{*}$ = deactivated form of $CuFe_2O_4$

Agglomeration and sedimentation of the photocatalyst particles will occur at a considerably high photocatalyst concentration. This condition will decrease the rate of degradation of methylene blue solution because of the reduction of the photocatalyst surface available for photon absorption and reactant adsorption (Sreethawong et al.,2007).

4.3.1.1 Effect of Fenton system

In the effort to ensure all the other parameters remain constant throughout the experiment to study the effect of fenton system, the experiment conditions were fixed to a catalyst loading of 1.0 g/L, 20 ppm of initial methylene blue concentration, similar photocatalytic reactor and visible light intensity as well as similar stirring speed using magnetic stirrer. The amount of hydrogen peroxide, H_2O_2 was varied to investigate the effect of fenton system in the photo-degradation of methylene blue solution. Six different amount of H_2O_2 were investigated viz. 0.001 ml, 0.005 ml, 0.01 ml, 0.05 ml, 0.1 ml and 0.5 ml. Subsequently, the corresponding result of photo-degradation of methylene blue is plotted in Figure 4-12 as a function of time.

Figure 4-12 illustrates the photocatalytic degradation of methylene blue at various amount of H_2O_2 as a function of time. The efficiency of photo-degradation increased significantly with the increasing amount of H_2O_2 added in the reaction mixture. The result showed that the increase in the amount of H_2O_2 from 0.001 ml to 0.5 ml significantly shortened the time necessary to degrade the methylene blue solution.

This is because with the addition of H_2O_2 as an oxidant, fenton system is created in which iron cations react with H_2O_2 to generate more free hydroxyl radical (·OH) which will subsequently react with methylene blue for degradation. The increase of H_2O_2 concentration generates more free-hydroxyl radicals which causes dye degradation (Banat et al., 2005). The mechanism is as shown in the following equations (Casbeer et al., 2012):

$$Fe^{2+} + H_2O_2 \rightarrow Fe^{3+} + OH^- + \cdot OH \qquad (4\text{-}9)$$

$$Fe^{2+} + H_2O_2 \rightarrow Fe^{2+} + \cdot OOH + H^+ \quad (4\text{-}10)$$

$$H_2O_2 + \cdot OH \rightarrow H_2O + \cdot OOH \quad (4\text{-}11)$$

$$H_2O_2 + e^- \rightarrow OH^- + \cdot OH \quad (4\text{-}12)$$

$$OH^- + h^+ \rightarrow H^+ + \cdot OH \quad (4\text{-}13)$$

There is also possibility that once ·OOH is formed, it reacts with Fe^{3+} to form O_2

$$Fe^{3+} + \cdot OOH \rightarrow Fe^{2+} + H^+ + O_2 \quad (4\text{-}14)$$

However, this reaction is less likely to occur in a reaction mixture that includes contaminants that are also being oxidized because there are competing reactions with generated ·OH (Costa et al., 2003).

Free hydroxyl radicals is the second most powerful oxidizing agent after fluorine (Mohabansi et al., 2011). Fenton system will further enhanced the generation of oxygen reactive species (·OH and ·OOH) which will then aid in the photo-degradation of methylene blue.

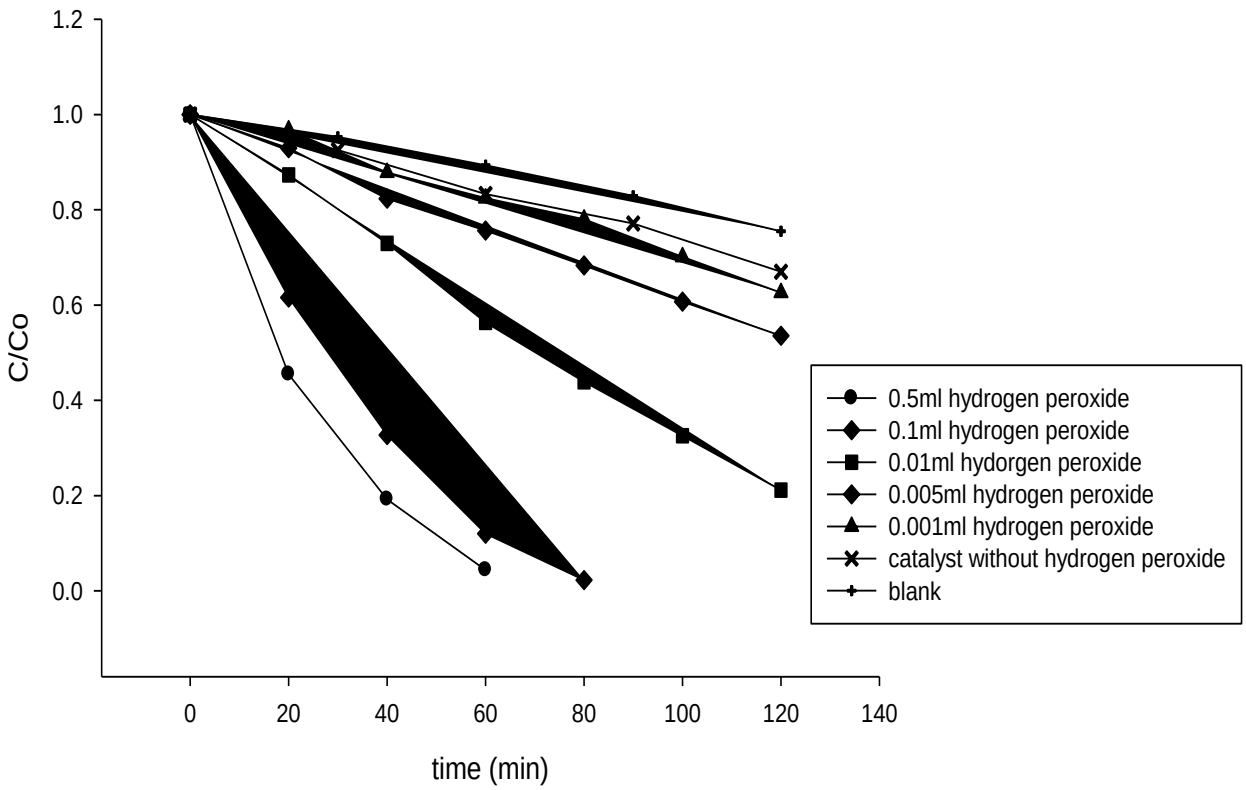

Figure 4-10: Photo-degradation of methylene blue at various amount of H_2O_2

4.3.1.2 Langmuir-Hinshelwood Model

Langmuir-Hinshelwood (L-H) kinetic model was applied for evaluation and comparison of heterogeneous catalytic systems. This kind of model can be expressed as:

$$r = \frac{dC}{dt} = \frac{kKC}{1+KC} \qquad (4\text{-}15)$$

Where

r = dC/dt = degradation rate of methylene blue (mg L^{-1} min^{-1})
k = reaction rate constant (ppm min g)$^{-1}$

C = concentration of methylene blue (ppm or mg L^{-1})
K = adsorption coefficient of reactant

When the concentration of methylene blue, C, is very small as portrayed in current work, the product of KC is negligible with respect to the unity so that the equation (4-15) can be further simplified into first-order kinetics equation as shown below:

$$\ln\left(\frac{Co}{C}\right) = kt \qquad (4\text{-}16)$$

where k is the apparent pseudo first order reaction rate constant. Figure 4-11 showed the apparent first order kinetic rate constant of experiment with different amount of H_2O_2. Table 4-4 summarizes the apparent first order rate constant, k and coefficient of determination, R^2.

It can be observed from Table 4-5 that the coefficient of determination, R^2 for all the experiment with different amount of H_2O_2 were greater than 0.9 which indicated that the kinetic degradation of methylene blue in Fenton system did follow pseudo first order mechanism. The values of apparent rate constant, k are listed in the same table. The apparent rate constant increased with the increasing amount of H_2O_2 added with the highest k value (48.1 x 10^{-3} /min) is 0.5 ml of H_2O_2 added in the reaction mixture. The

highest k values means that it has the highest performance in the degradation of methylene blue solution which is compatible to the result and discussion in Section 4.3.1.1. The photo-degradation of methylene blue increases with the increasing amount of H_2O_2 added in the reaction mixture.

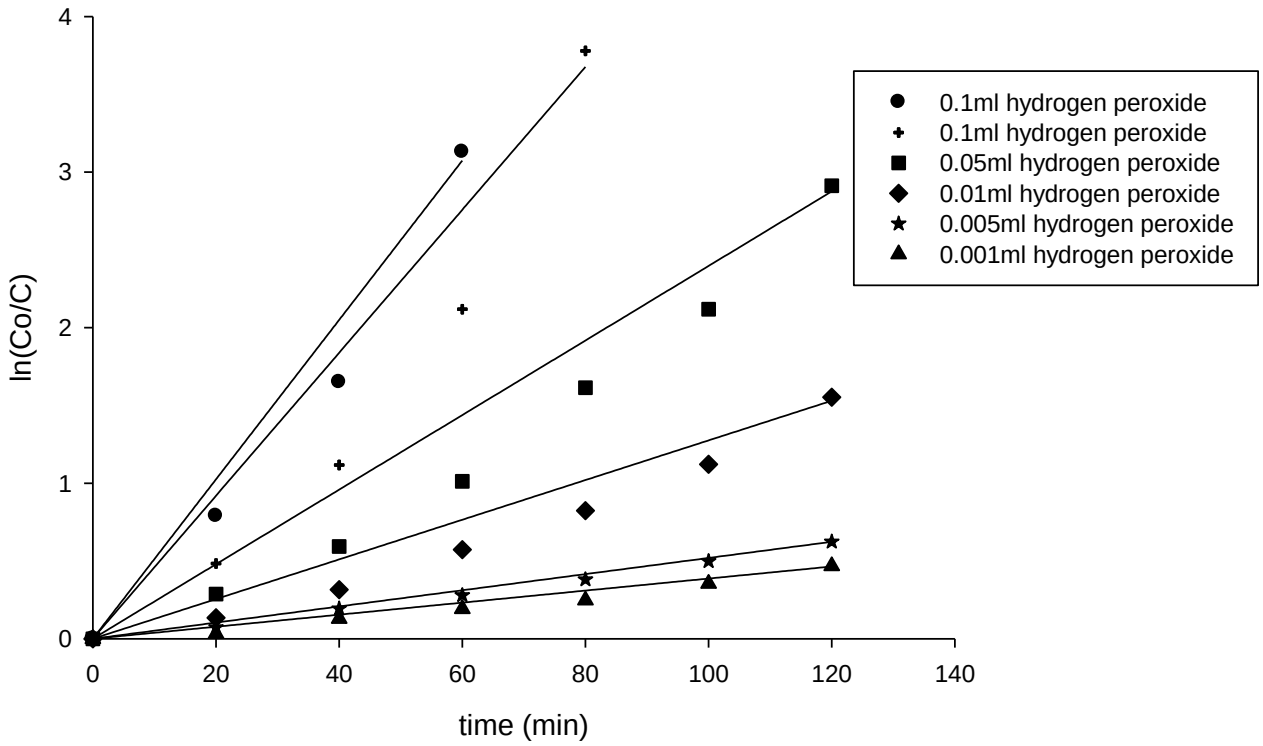

Figure 4-11: Apparent first order kinetic rate constant of experiment with different amount of H_2O_2

Table 4-5: Summary of apparent first order rate constant and coefficient of determination

Amount of H_2O_2, ml	Apparent rate constant, k($\times 10^{-3}$ min^{-1})	Coefficient of determination, R^2
0.5	48.1	0.97
0.1	40.3	0.92
0.05	21.4	0.96
0.01	11.4	0.96

0.005	5	0.99
0.001	3.5	0.97

4.3.2 Photocatalytic-degradation of Glycerol

Methylene blue and glycerol share the similar properties that both of them are organic compound. Due to the effectiveness of $CuFe_2O_4$ in the photo-degradation of methylene blue dye, its photocatalytic degradation of glycerol solution was also explored.

The effect of photocatalyst in the glycerol solution on the rate of photo-degradation was examined at a catalyst loading of 2 g/L. Figure 4-12 reveals the graph of glycerol photo-degradation with and without $CuFe_2O_4$. It can be demonstrated that neither visible light alone nor the presence of $CuFe_2O_4$ was capable to photo-degrade the glycerol solution. One of the plausible reasons is that there are insufficient generation of hydroxyl free radicals to degrade the glycerol. Therefore, H_2O_2 was added in the reaction mixture to increase the production of hydroxyl free radicals in which the Fenton system was established.

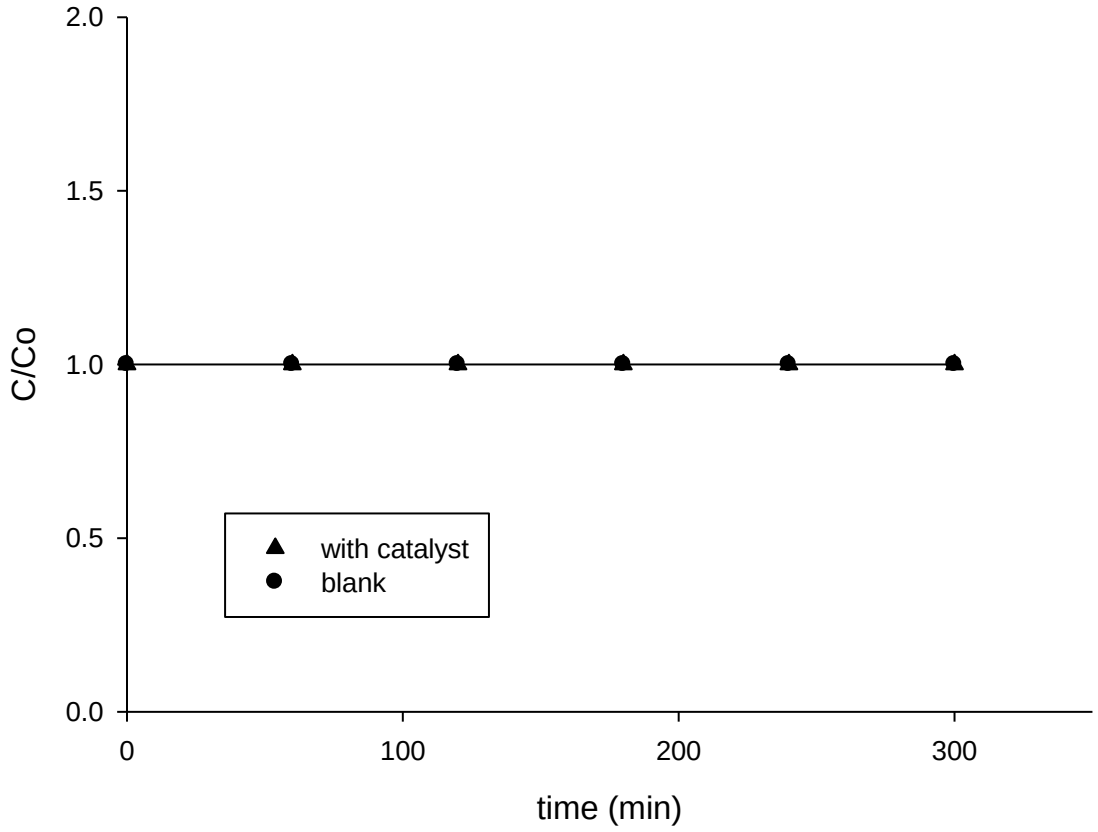

Figure 4-12: Glycerol photo-degradation with and without $CuFe_2O_4$

The experiment with different amount of H_2O_2 (0.1 ml, 0.5 ml, and 1 ml) was examined with a fixed catalyst loading of 2g/L on 0.5 v/v% glycerol solution. The result is shown in Figure 4-13.

From the result shown, it can be seen that the experiment with only $CuFe_2O_4$ and visible light irradiation showed no effect towards the glycerol degradation. However, there was photo-degradation of glycerol solution under visible light irradiation after adding certain amount of H_2O_2 which were 0.1 ml, 0.5 ml and 1.0 ml in the sample mixture. This were due to the increase in the production of hydroxyl free radicals that would eventually degrade the glycerol. The photo-degradation of glycerol was faint with the addition of 0.1 ml of H_2O_2. On the other hand, as the amount of H_2O_2 increased, more hydroxyl free radicals were produced, hence, it can be seen that the photo-degradation of glycerol solution increased significantly after the amount of H_2O_2 was increased. The mechanism

is similar to the Fenton system in the photo-degradation of methylene blue which was shown in the Equation 4-9 to 4-13.

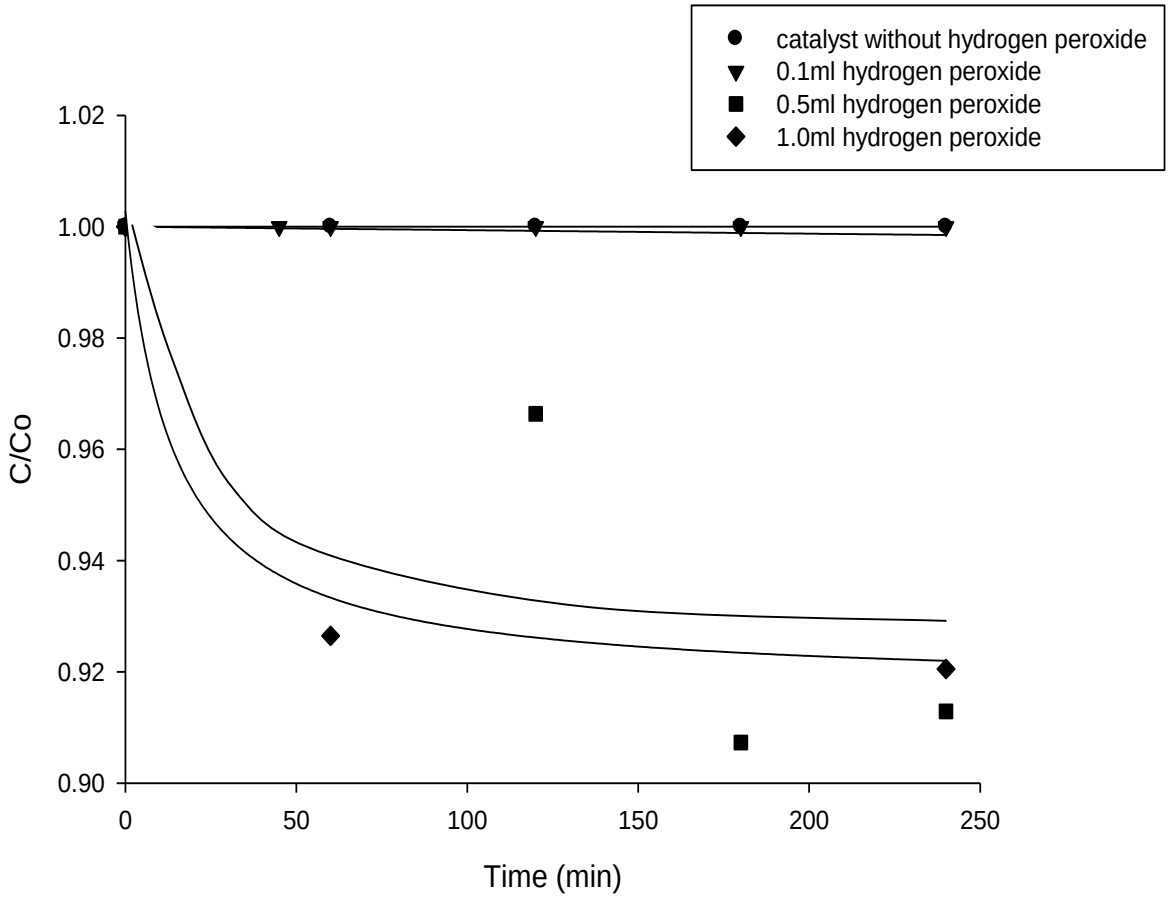

Figure 4-13: photo-degradation of glycerol solution with different amount of H_2O_2

CHAPTER 5

5 CONCLUSIONS AND RECOMMENDATIONS

5.1 Conclusions

In summary, photocatalytic degradation of methylene blue and glycerol aqueous solution over copper ferrite catalyst was studied and investigated. The photocatalyst, $CuFe_2O_4$ was successfully synthesized by co-precipitation method. Subsequently, the synthesized photocatalyst was subjected to structural characterization with XRD, N_2-physisorption, FESEM and gas pycnometer.

The prepared $CuFe_2O_4$ has face-centred cubic crystal system and possessed spinel structure as evinced by the XRD analysis. From the N_2 physisorption analysis, the BET specific surface area of calcinated $CuFe_2O_4$ photocatalyst was 102.37 cm^2 /g. The pore volume at $P/P_o = 0.95$ was determined to be 0.17 cm^3 /g. On top of that, the morphology of the photocatalyst which was captured by FESEM showed the homogeneity and uniformity of particle sizes. The $CuFe_2O_4$ particlesexhibited branched structures with rod shapes. The size was lower than 1 µm. Besides, the density of synthesized photocatalyst was analysed from gas pycnometer and the density was 2.50 g/cm^3 from the average of three values.

For the photocatalytic degradation study on methylene blue, the synthesized $CuFe_2O_4$ was an effective photocatalyst as it was visible light-responsive. The catalyst loading has been found to affect the efficiency of MB photo-degradation. In this study, the degradation with 1.0 g/L catalyst loading was more efficient than 0.5 g/L catalyst loading. This is due to the more available active site of photocatalyst. Moreover, it can further enhance the photo-degradation of methylene blue solution by the addition of H_2O_2 at where Fenton system is established. The result showed that the photo-degradation increases with the increasing amount of H_2O_2 added. Addition of 0.5 ml of H_2O_2 showed the best performance of MB photo-degradation. Besides, Langmuir-Hinshelwood model was used to describe the photocatalytic activity of $CuFe_2O_4$. The kinetic data obtained from the

photocatalytic degradation of methylene blue fitted well with the pseudo first-order kinetic model.

On the other hand, the synthesized photocatalyst showed no effect to the photo-degradation of glycerol solution unless certain amount of H_2O_2 was added for the case of glycerol photo-degradation. The result showed that, as the amount of H_2O_2 added increased, the photo-degradation of glycerol solution also increased. In this study, the addition of 1 ml of H_2O_2 exhibited superior glycerol decomposition.

In a nutshell, the aim to synthesize, characterize and perform photocatalytic degradation study on methylene blue and glycerol solution is a success.

5.2 Recommendations

Since $CuFe_2O_4$ shows good performance on the degradation of methylene blue, future work on treating actual dyes problem should be carried out for the wastewater purification purposes. Besides, for the case of glycerol solution, proper method regarding the photocatalyst preparation should be revised to improve the reactivity of photocatalyst towards the photo-degradation of glycerol.

6 REFERENCES

(2013, November 20). Retrieved from MATERIAL SAFETY DATA SHEET : http://www.aquasonic.com.au/wp-content/uploads/pdf/MethyleneBlue.pdf

Adedayo, O., Javadpour, S., Taylor, C., Anderson, W., & Moo, Y. M. (2004). Decolourization and detoxification of methyl red by aerobic bacteria from a wastewater treatment plant. *World Journal of Microbiology and Biotechnology (20)*, 545-550.

Ahmed, Y. M., Hessien, M. M., Rashad, M. M., & Ibrahim, I. A. (2009). Nano-crystalline copper ferrites from secondary iron oxide (mill scale). *Journal of Magnetism and Magnetic Materials (321)*, 181-187.

Alexandre Bevilacqua Leoneti, Valquiria Aragão-Leoneti, Sonia Valle Walter Borges de Oliveira. (2012). Glycerol as a by-product of biodiesel production in Brazil: Alternatives for the use of unrefined glycerol. *Renewable Energy(45)*, 138–145.

Ayoub, M., & Abdullah, A. Z. (2012). Critical review on the current scenario and significance of crude glycerol resulting. *Renewable and Sustainable Energy Reviews(16)*, 2671-2686.

Banat, F., Al-Asheh, S., Al-Rawashdeh, M., & Nusair, M. (2005). Photodegradation of methylene blue dye by the UV/H202 and UV/acetone oxidation processes . *Desalination (181)*, 225-232.

Barbara, L. D., & Christine, M. C. (2012). *X-ray powder diffraction.*

Braunauer, S., Emmet, P. H., & Teller, E. (1938). Adsorption of Gases in Multimolecular Layer. *J Amer Chem Soc (60)*, 309-319.

Brit. (2008, June 18). Synthetic Dyes: A look at Environmental & Human Risks.

Casbeer, E., Sharma, V. K., & Li, X. Z. (2012). Synthesis and photocatalytic activity of ferrites under visible light: A review. *Separation and Purification Technology*, 1-14.

Chequer, F. M., Oliveira, G. A., Ferraz, E. R., Cardoso, J. C., Zanoni, M. V., & Oliveira, D. P. (2013). *Eco-friendly textile dyeing and finishing.* Intech.

Choi, W., Termin, A., & Hoffmann, M. R. (1994). The Role of Metal Ion Dopants in Quantum-Sized TiO2: Correlation between Photoreactivity and Charge Carrier Recombination Dynamics. *J. Phys. Chem (98)*, 13669-13679.

Chong, M. N., Jin, B., Chow, C. W., & Saint, C. (2010). Recent developments in photocatalytic water treatment. *water research (44)*, 2997-3027.

Daniele Misturini Rossi, Janaına Berne da Costa, Elisangela Aquino de Souza,Maria do Carmo Ruaro Peralba, Dimitrios Samios, Marco Antonio Zachia Ayub. (2011). Comparison of different pretreatment methods for hydrogen production using environmental microbial consortia on residual glycerol from biodiesel. *International Journal of Hydrogen Energy (36)*, 4814–4819.

De Laat, J., Truong, L. G., & Legube, B. (2004). A comparative study of the effects of chloride, sulfate and nitrate ions on the rates of decomposition of H2O2 and organic compounds by Fe(II)/H2O2 and Fe(III)/H2O2. *Chemosphere (5)*, 715-723.

Ding, X. A. (2014). A dual-cell wastewater treatment system with combining anodic visible light driven photoelectro-catalytic oxidation and cathadic electro-Fenton oxidation. *Separation and Purification Technology, vol 125*, 103-110.

Erik Casbeer, Virender K. Sharma,Xiang-Zhong Li. (2012). Synthesis and photocatalytic activity of ferrites under visible light: A review. *Separation and Purification Technology (87)*, 1-14.

Fan, H., Zhou, L., Jiang, X., Huang, Q., & Lang, W. (2014). Adsorption of Cu2 + and methylene blue on dodecyl sulfobetaine surfactant-modified montmorillonite. *Applied Clay Science (95)*, 150-158.

Ghahremanzadeh, R., Rashid, Z., Zarnani, A.-H., & Naeimi, H. (2014). Highly active magnetically separable CuFe2O4 nanocatalyst: an efficient catalyst for the green synthesis of tetrahydrofuro[3,4-b]quinoline-1,8(3H,4H) dione derivatives. *J IRAN CHEM SOC (11)*, 1407-1419.

Haihua Yanga, Jianhui Yana, Zhouguang Lua, Xiang Chenga, Yougen Tang. (2009). Photocatalytic activity evaluation of tetragonal CuFe2O4 nanoparticles for the H2. *Journal of Alloys and Compounds (476)*, 715-719.

Hasliza Bahruji, Michael Bowker, Philip R. Davies, Layla Saeed Al-Mazroai, Amanda Dickinson,. (2010). Sustainable H2 gas production by photocatalysis. *Journal of Photochemistry and Photobiology A: Chemistry(216)*, 115–118.

Hidawati. E.N., &. Sakinah. A.M.M. (2011). Treatment of glycerin pitch from biodiesel production. *International Journal of Chemical and Environmental Engineering(5)*, 309-314.

Kazuhiko Maeda, and Kazunari Domen. (2007). New Non-Oxide Photocatalysts Designed for Overall Water Splitting under Visible Light. *The Journal Of Physical Chemistry (22)*, 7851-7861.

Keng, E. Y. (1969). Air and helium pycnometer. *Powder technology (3)*, 179-180.

Khosravi, I., & Eftekhar, M. (2014). Na0.5Li0.5CoO2 nanopowders: Facile synthesis, characterization and their application for the removal of methylene blue dye from aqueous solution (25). *Advanced Powder Technology*, 1721-1727.

Kogo, K., Yoneyama, H., & Tamura, H. (1980). Photocatalytic oxidation of cyanide on platinized titanium dioxide. *The Journal of Physical Chemistry (84)*, 1705-1710.

Kondarides, D. I., Daskalaki, V. M., Patsoura, A., & Verykios, X. E. (2008). Hydrogen Production by Photo-Induced Reforming of Biomass Components and Derivatives at Ambient Conditions. *Catal Lett (122)*, 26-32.

Lachheb, H., Puzenat, E., Houas, A., Ksibi, M., Elaloui, E., Guillard, C., & Hermann, J. M. (2002). Photocatalytic degradation of various types of dyes (Alizarin S, Crocein Orange G, Methyl Red, Congo Red, Methylene Blue) in water by UV-irradiated titania. *Applieed catalysis B: Environmental (39)*, 75-90.

Leoneti, A. B., Leoneti, V. A., & Oliveira, S. V. (2012). Glycerol as a by-product of biodiesel production in Brazil: Alternatives for the use. *Renewable Energy(45)*, 138-145.

Mahmoodi, N. M. (2011). Photocatalytic ozonation of dyes using copper ferrite nanoparticle prepared by co-precipitation method. *Desalination (279)*, 332-337.

Melo, M. d., & Silva, L. A. (2011). Visible light-induced hydrogen production from glycerol aqueous solution on hybrid Pt–CdS–TiO2 photocatalysts. *Journal of Photochemistry and Photobiology A: Chemistry (226)*, 36-41.

Meng, Z., & Juan, Z. (2008). Wastewater treatment by photocatalytic oxidation of Nano-ZnO. *Global Environmental Policy in Japan (12)*, 1-9.

Michler, G. H. (2004). *Electron microscopy of polymers.* Berlin Heidelberg: Springer.

N.N.A.N. Yusuf, S.K. Kamarudin, Z. Yaakub. (2011). Overview on the current trends in biodiesel production. *Energy Conversion and Management(56)*, 2741–2751.

Naseri, M. G., Saion, E. B., Ahangar, H. A., & Shaari, A. H. (2013). Fabrication, characterization, and magnetic properties of copper ferrite nanoparticles prepared by a simple, thermal-treatment method. *Materials research bulletin (48)*, 1439-1446.

Ogugbue, C. J., & Sawidis, T. (2011). Bioremediation and detoxification of synthetic wastewater containing triarylmethane dyes by aeromonas hydrophila isolated from industrial effluent. *Biotechnology Research International (2011)*, 11.

Ohama, Y., & Gemert, D. V. (2011). *Application of Titanium Dioxide Photocatalysis to Construction Materials* . New York: Springer.

P.P.Edwards, V.L.Kuznetsov, W.I.F.David , N.P.Brandon. (2008). Hydrogen and fuel cells: Towards a sustainable energy future. *Energy Policy(36)*, 4356–4362.

Pignatello, J. J., Liu, D., & Huston, P. (1992). Dark and photoassisted iron(3+)-catalyzed degradation of chlorophenoxy herbicides by hydrogen peroxide. *Environ. Sci. Technol (26)*, 944-951.

Prescott, S. C., & Dunn, C. G. (1959). *Industrial Microbiology.* New York: McGraw-Hill.

Sing, K. S., Everett, D. H., Haul, R. A., Moscou, L., Pierotti, R. A., Rouquerol, J., & Siemieniewska, T. (1985). REPORTING PHYSISORPTION DATA FOR GAS/SOLID SYSTEMS with Special Reference to the Determination of Surface Area and Porosity. *International union of pure and applied chemistry (57)*, 603-619.

Spencer, J. (2007, August 22). China Pays Steep Price As Textile Exports Boom. Dongguan, China.

Tan, H. W., Abdul Aziz, A. R., & Aroua, M. K. (2013). Glycerol production and its applications as a raw material : A review. *Renewable and Sustainable Energy Reviews (27)*, 118-127.

Tatyana P. Lyubina, Dina V. Markovskaya,Ekaterina A. Kozlova, Valentin N. Parmon. (2013). Photocatalytic hydrogen evolution from aqueous solutions of glycerol under visible light irradiation. *International Journal of Hydrogen Energy(38)*, 14172-14179.

ThanhThuy, T. T., Feng, H., & Cai, Q. (2013). Photocatalytic degradation of pentachlorophenol on ZnSe/TiO2 supported by photo-Fenton system. *Chemical Engineering Journal (223)*, 379-387.

Uddin, M. R., Kham, M. R., Rahman, M. W., Yousuf, A., & Cheng, C. K. (2014). Synthesis, characterization and activity evaluation of visible light responsive CuFe2O4 catalyst. *8th MUCET 2014.* Melaka, Malaysia.

Umar, M., & Abdul Aziz, H. (2013). *Photocatalytic Degradation of Organic Pollutants in Water.* Intech.

Wang, L., Zheng, J., Gong, X., Hartman , R., & Antonucci, V. (2014). Efficient HPLC method development using structure-based database search, physico-chemical prediction and chromatographic simulation. *Journal of pharmaceutical and biomedical analysis (104)*, 49-54.

Wang, S., Zhu, Z. H., Coomes, A., Haghseresht, F., & Lu, G. Q. (2005). The physical and surface chemical characteristics of activated carbons and the adsorption of methylene blue from wastewater. *Journal of Colloid and Interface Science (284)*, 440-446.

Wang, Z. X., Zhuge, J., Fang, H., & Prior, B. A. (2001). Glycerol production by microbial fermentation:A review. *Biotechnology Advances (19)*, 201-223.

Yang, H., Yan, J., Lu, Z., Cheng, X., & Tang, Y. (2009). Photocatalytic activity evaluation of tetragonal CuFe2O4 nanoparticles for the H2 evolution under visible light irradiation. *Journal of Alloys and Compounds (476)*, 715-719.

Yang, X., Ma, F., Li, K., Guo, Y., Hu, J., Li, W., . . . Guo, Y. (2010). Mixed phase titania nanocomposite codoped with metallic silver and vanadium oxide: New

efficient photocatalyst for dye degradation. *Journal of Hazardous Materials (175)*, 429-438.

Yong, K. C., Ooi, T. L., Dzulkefly, K., WanYunus, W., & Hazimah, A. H. (2001). Characterization of Glycerol Residue From a Palm Kernel Oil Methyl Ester Plant. *Journal of Oil Palm Research(13)*, 1-6.

Yu, J. C., Yu, J., Ho, W., Jiang, Z., & Zhang, L. (2002). Effects of F- Doping on the Photocatalytic Activity and Microstructures of Nanocrystalline TiO2 Powders. *Chem. Mater (14)*, 3808-3816.

Yusuf, N. N., Kamarudin, S. K., & Yaakub, Z. (2011). Overview on the current trends in biodiesel production. *Energy Conversion and Management(52)*, 2741-2751.

7 APPENDICES

Gas Pycnometer

Combined Report

Summary Report

Sample Volume
Average: 0.1632 cm³
Standard Deviation: 0.0001 cm³

Sample Density
Average: 2.4953 g/cm³
Standard Deviation: 0.0021 g/cm³

Tabular 1

Cycle#	P1 Pressure (psig)	P2 Pressure (psig)	Volume (cm³)	Density (g/cm³)	Total Pore Volume (cm³/g)
1	19.903	4.588	0.1634	2.4928	0.5988
2	19.941	4.597	0.1631	2.4979	0.5997
3	19.899	4.587	0.1632	2.4953	0.5992

Summary Data	Average	Standard Deviation
Volume:	0.1632 cm³	0.0001 cm³
Density:	2.4953 g/cm³	0.0021 g/cm³

6202- Total solids concentration is invalid; liquid density is greater-than or equal to solids density.

Tabular 2

Cycle#	P1 Pressure (psig)	P2 Pressure (psig)	Volume (cm³)	Density (g/cm³)	Total Pore Volume (cm³/g)
1	19.903	4.588	0.1634	2.4928	0.5988
2	19.941	4.597	0.1631	2.4979	0.5997
3	19.899	4.587	0.1632	2.4953	0.5992

Summary Data	Average	Standard Deviation
Volume:	0.1632 cm³	0.0001 cm³
Density:	2.4953 g/cm³	0.0021 g/cm³

6202- Total solids concentration is invalid; liquid density is greater-than or equal to solids density.

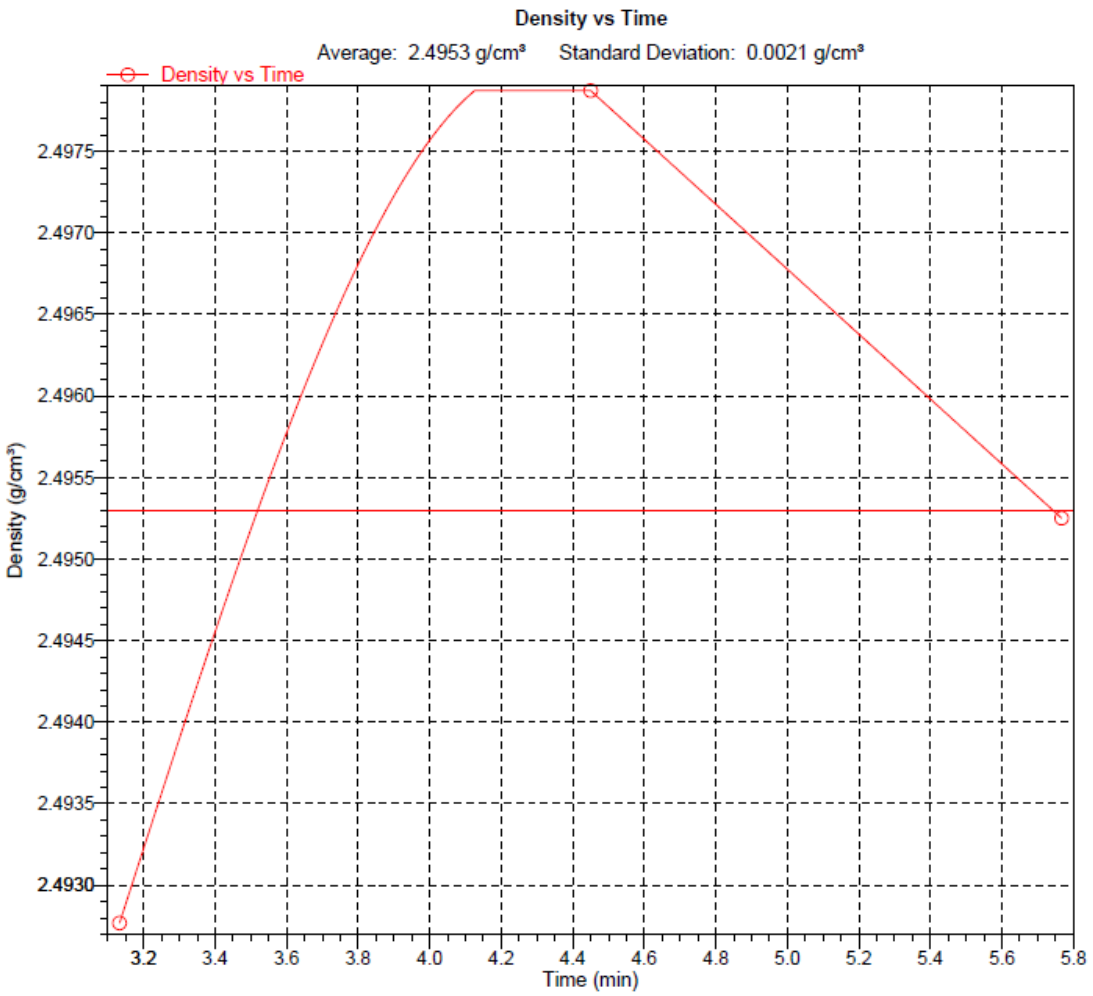
Density vs Time
Average: 2.4953 g/cm³ Standard Deviation: 0.0021 g/cm³
Density vs Time
Density (g/cm³)
2.4975
2.4970
2.4965
2.4960
2.4955
2.4950
2.4945
2.4940
2.4935
2.4930
3.2
3.4
3.6
3.8
4.0
4.2
4.4
4.6
4.8
5.0
5.2
5.4
5.6
5.8
Time (min)

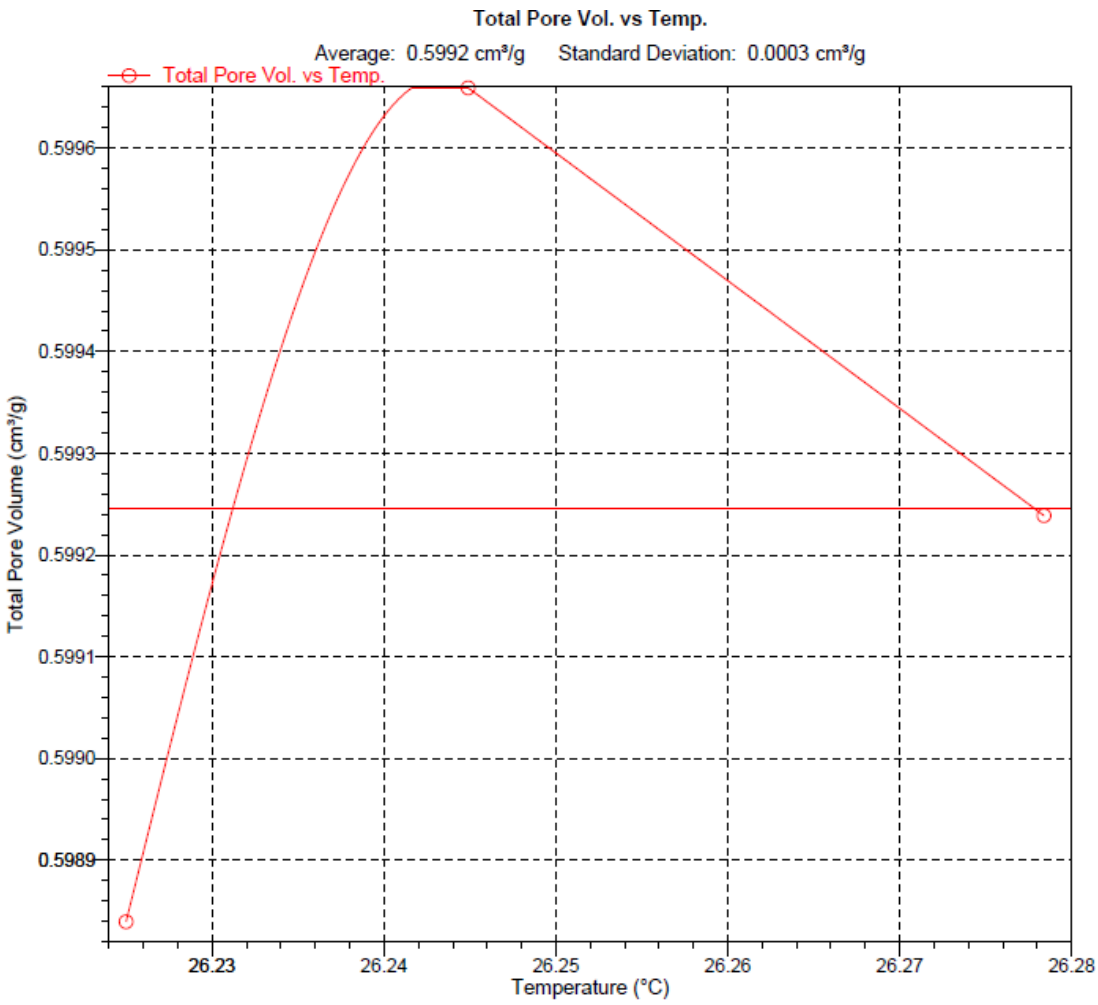
Total Pore Vol. vs Temp.
Average: 0.5992 cm³/g Standard Deviation: 0.0003 cm³/g
Total Pore Vol. vs Temp.
Total Pore Volume (cm³/g)
0.5996
0.5995
0.5994
0.5993
0.5992
0.5991
0.5990
0.5989
26.23
26.24
26.25
26.26
26.27
26.28
Temperature (°C)

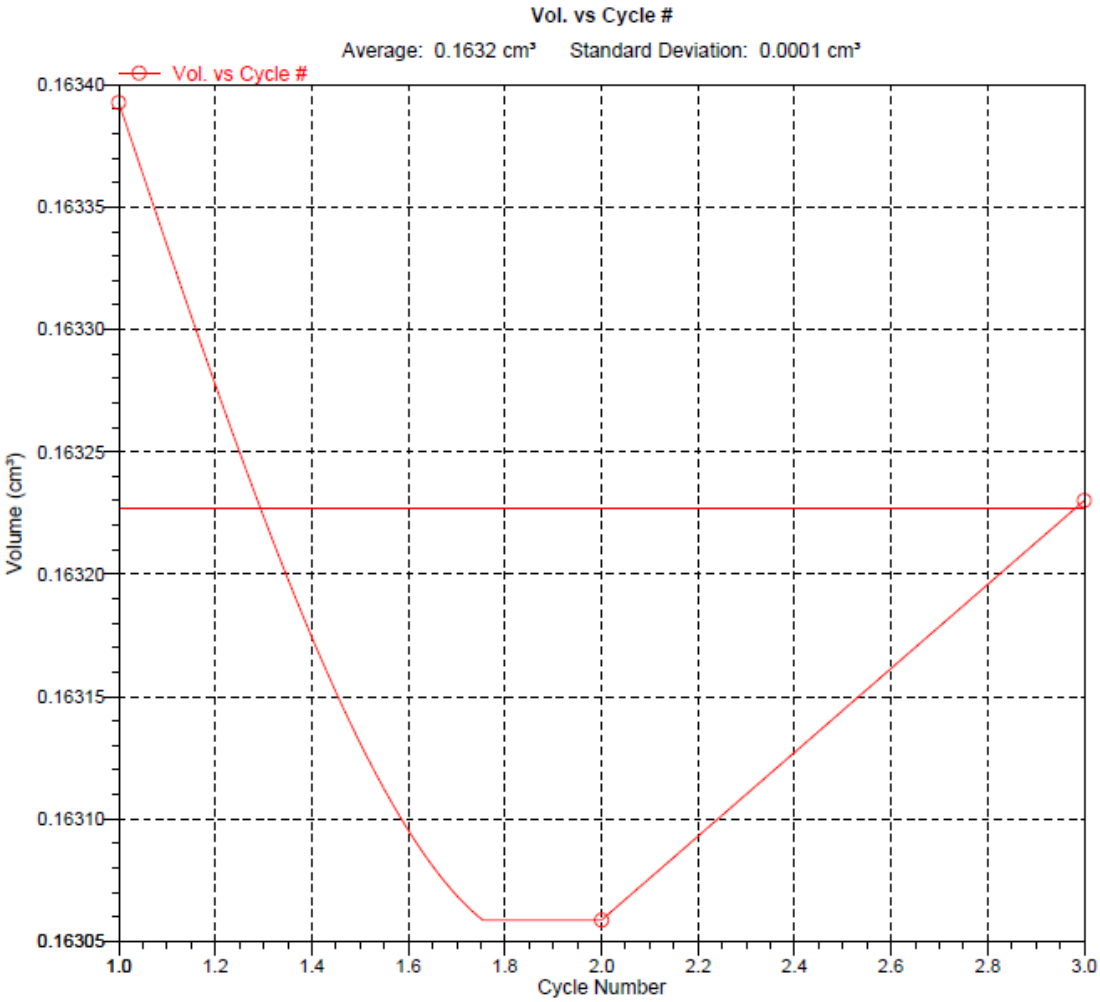
Vol. vs Cycle #
Average: 0.1632 cm³ Standard Deviation: 0.0001 cm³
Vol. vs Cycle #
0.16340
0.16335
0.16330
0.16325
0.16320
0.16315
0.16310
0.16305
Volume (cm³)
1.0
1.2
1.4
1.6
1.8
2.0
2.2
2.4
2.6
2.8
3.0
Cycle Number

X-ray Diffraction (XRD)

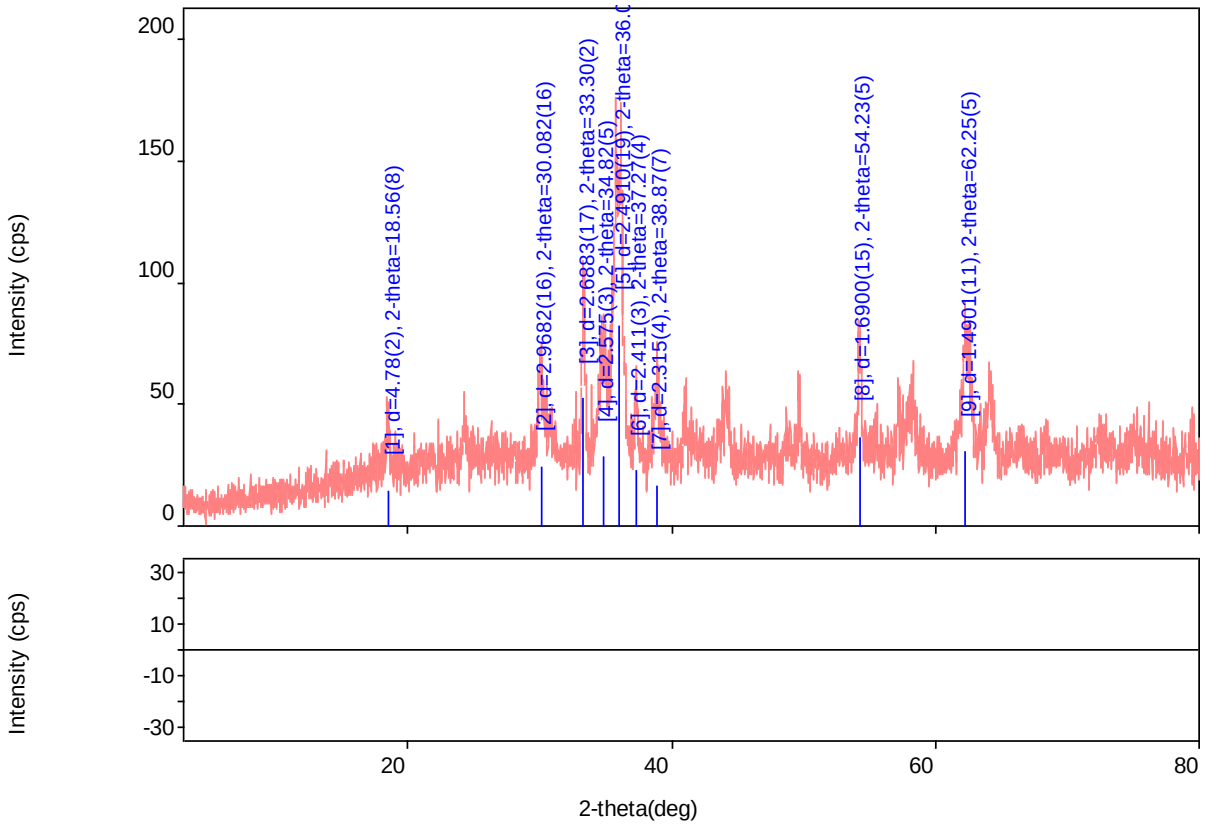

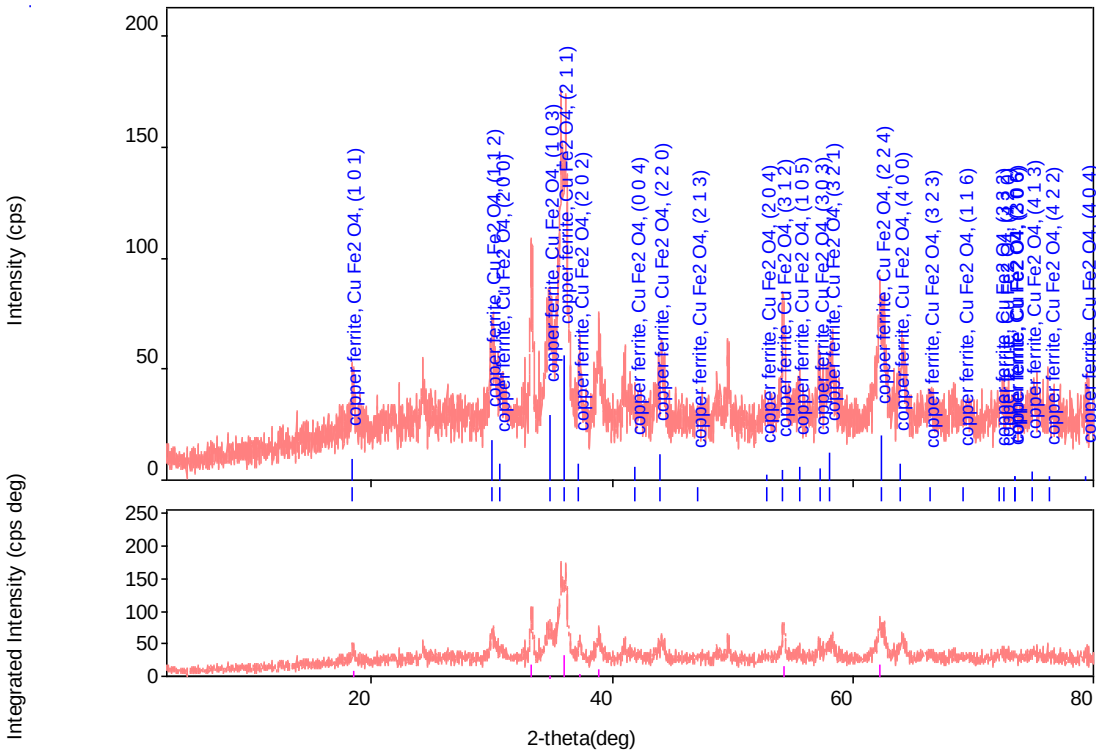

Nitrogen Physisorption (BET)

Adsorption Data

#	V_{dos} [cm^3]	p_{load} [Torr]	p_{equi} [Torr]	t_{equi} [min:s]	p^0 [Torr]	p/p^0	V_{ads} [cm^3g^{-1}]	n_{ads} [mmol g^{-1}]
1						6.4E-5	1.9641	0.1624
2						0.00012	8.1508	0.6738
3						0.0025	13.787	1.1398
4						0.0178	17.313	1.4313
5						0.0599	20.7	1.7113
6						0.1161	23.782	1.966
7						0.1767	26.702	2.2074
8						0.2385	29.618	2.4485
9						0.2982	32.557	2.6914
10						0.3576	35.674	2.949
11						0.4172	39.203	3.2408
12						0.4775	43.456	3.5924
13						0.533	48.362	3.998
14						0.5868	54.503	4.5056
15						0.6381	62.344	5.1538
16						0.6847	71.764	5.9326
17						0.7275	81.768	6.7595
18						0.768	89.939	7.435
19						0.8124	95.731	7.9139
20						0.8631	100.2	8.2833
21						0.9163	104.7	8.6557
22						0.9624	110.57	9.1405
23						0.9834	116.61	9.6395
24						0.9982	122.63	10.138
25						0.9998	129.35	10.693
26						1	137.89	11.399

Desorption Data

#	V_{dos} [cm^3]	p_{equi} [Torr]	t_{equi} [min:s]	p^0 [Torr]	p/p^0	V_{ads} [cm^3g^{-1}]	n_{ads} [mmol g^{-1}]
27					0.9978	131.97	10.91
28					0.9903	124.37	10.281
29					0.9773	118.59	9.8036
30					0.9581	113.72	9.4007
31					0.9316	109.95	9.0893
32					0.8956	106.8	8.8286
33					0.8469	103.5	8.5558
34					0.7934	100.28	8.2899
35					0.7393	97.091	8.0263
36					0.6921	92.722	7.6651
37					0.6596	86.856	7.1802
38					0.6391	81.217	6.7141
39					0.6234	76.242	6.3028
40					0.6088	71.238	5.8891
41					0.5961	66.911	5.5314
42					0.5826	62.742	5.1868
43					0.5652	58.24	4.8145
44					0.5466	53.911	4.4567
45					0.521	49.652	4.1046
46					0.4892	45.714	3.7791
47					0.4467	41.734	3.4501
48					0.3979	38.225	3.16
49					0.3456	35.16	2.9066
50					0.292	32.396	2.6781
51					0.2365	29.657	2.4517
52					0.1807	27.015	2.2333
53					0.1297	24.578	2.0318

Surface Area (Langmuir)

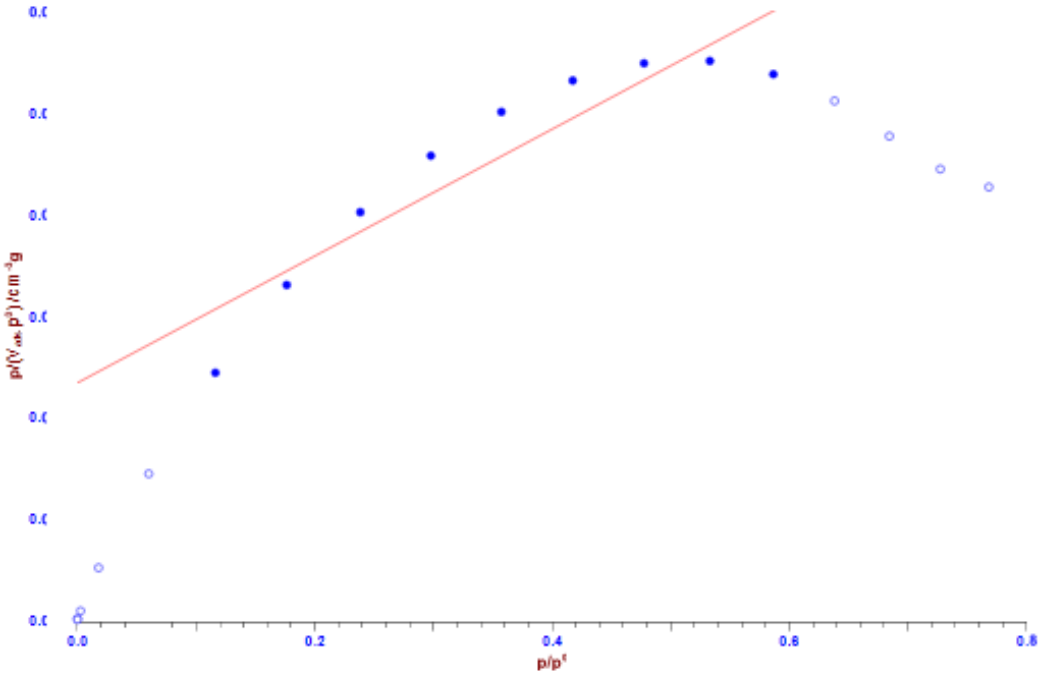

Linear regression from p/p^0 0.1 to 0.6

Offset: 0.00467752 ± 0.00074553

Slope: 0.01251057 ± 0.00192582

R: 0.92613526

Monoloayer volume 79.932 cm^3g^{-1}

Monoloayer amount: 3.5662 mmol g^{-1}

B: 2.6746

Calculation with a molecular area of 16.2 $Å^2$

Surface area was: 347.92 m^2g^{-1}

Surface Area (B.E.T.) 2 Parameters Line

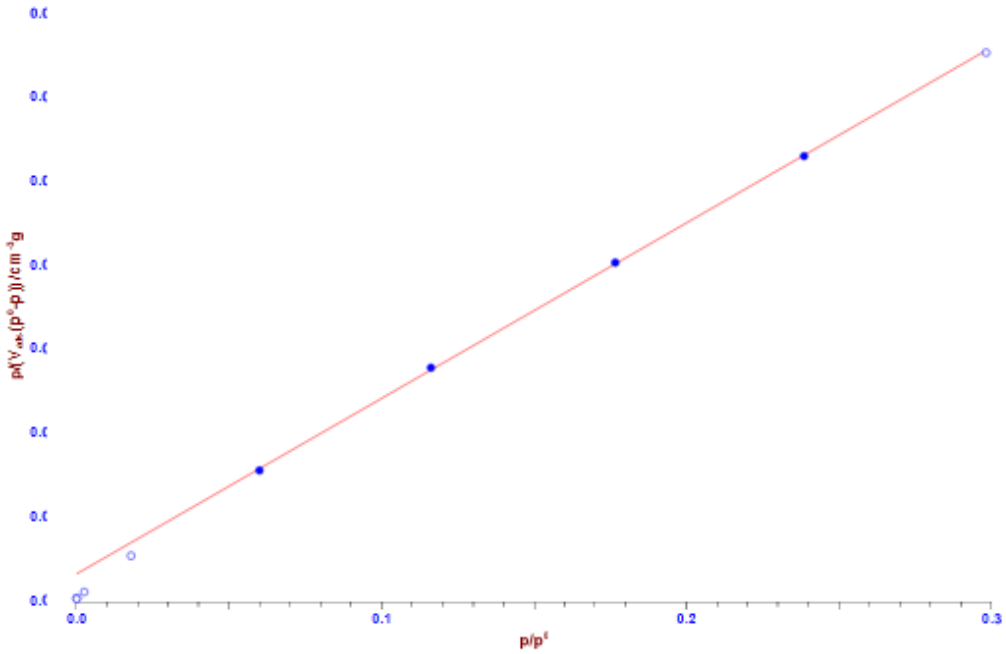

Linear regression from p/p^0 0.05 to 0.25

Offset: 0.0006085 ± 6.42229E-5

Slope: 0.04191188 ± 0.00039611

R: 0.99991069

Monoloayer volume 23.518 cm^3g^{-1}

Monoloayer amount: 1.0493 mmol g^{-1}

C: 69.877

Calculation with a molecular area of 16.2 $Å^2$

Surface area was: 102.37 m^2g^{-1}

Surface Area (B.E.T.) 3 Parameters Fit

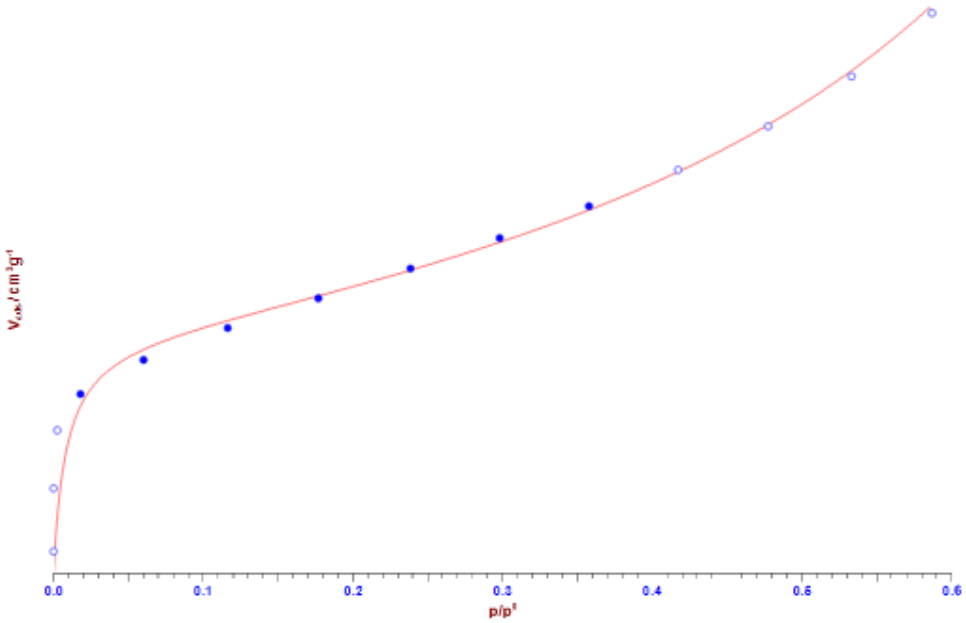

Simplex fit from p/p^0 0.005 to 0.4
r^2: 0.99044181

Monoloayer volume 22.996 cm^3g^{-1}
Monoloayer amount: 1.026 mmol g^{-1}
C: 121.62
N: 16.663

Calculation with a molecular area of 16.2 $Å^2$
Surface area was: 100.1 m^2g^{-1}

Mesopores (B.J.H.)

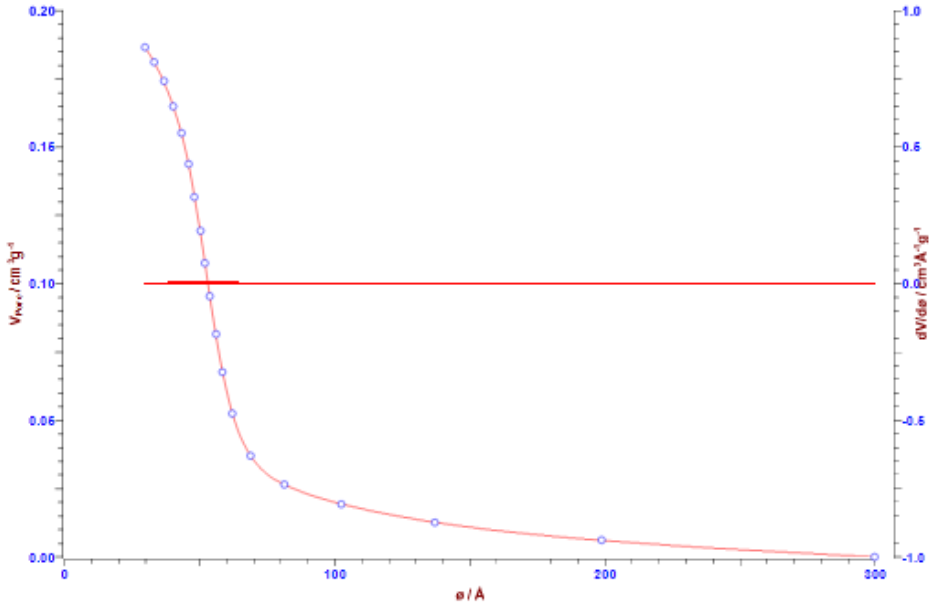

Calculations used Desorption Branch from p/p^0 0.3 to 0.95
with standard isotherm: Universal (Halsey)
from literature: ASTM Standards Designation: D 4641-87

Calculation with a molecular area of	16.2 $Å^2$
molecular weight of	28.01 g/mol
liquid density of	0.8086 g cm^{-3}
and surface tension of	8.85 Dyne cm^{-1}
Median pore diameter	54.034 Å
Maximum pore diameter	52.67 Å
Cumulative pore volume	0.1866 cm^3g^{-1}
Cumulative pore area	136.13 m^2g^{-1}

Mesopores (Cranston and Inkley)

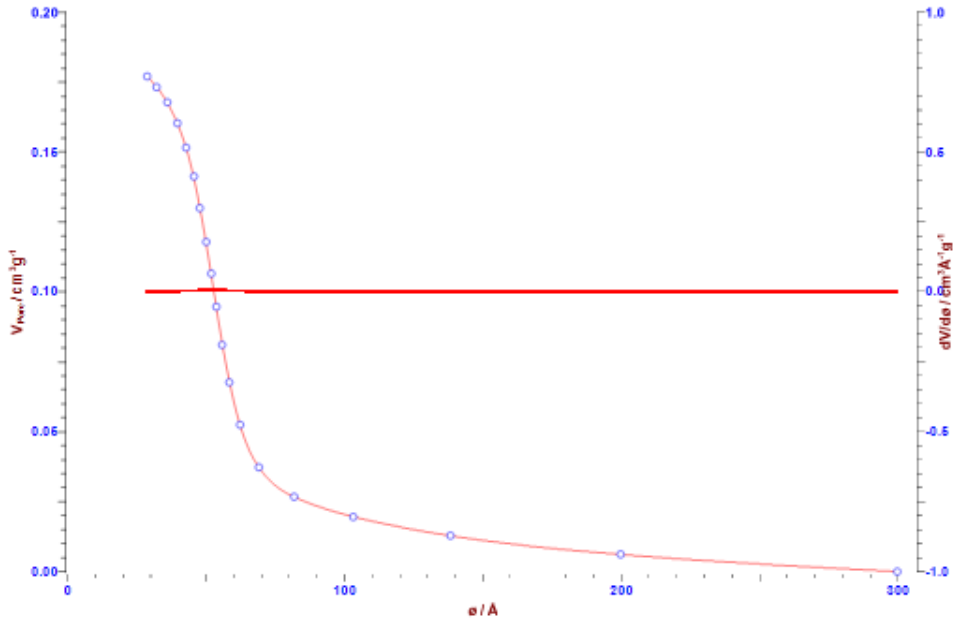

Calculations used Desorption Branch from p/p^0 0.3 to 0.95
with standard isotherm: Universal (Harkins,Jura)
from literature: ASTM Standards Designation: D 4641-87

Calculation with a molecular area of	16.2 $Å^2$
molecular weight of	28.01 g/mol
liquid density of	0.8086 g cm^{-3}
and surface tension of	8.85 Dyne cm^{-1}
Median pore diameter	54.574 Å
Maximum pore diameter	52.632 Å
Cumulative pore volume	0.177 cm^3g^{-1}
Cumulative pore area	127.11 m^2g^{-1}

Mesopores (Cranston and Inkley)

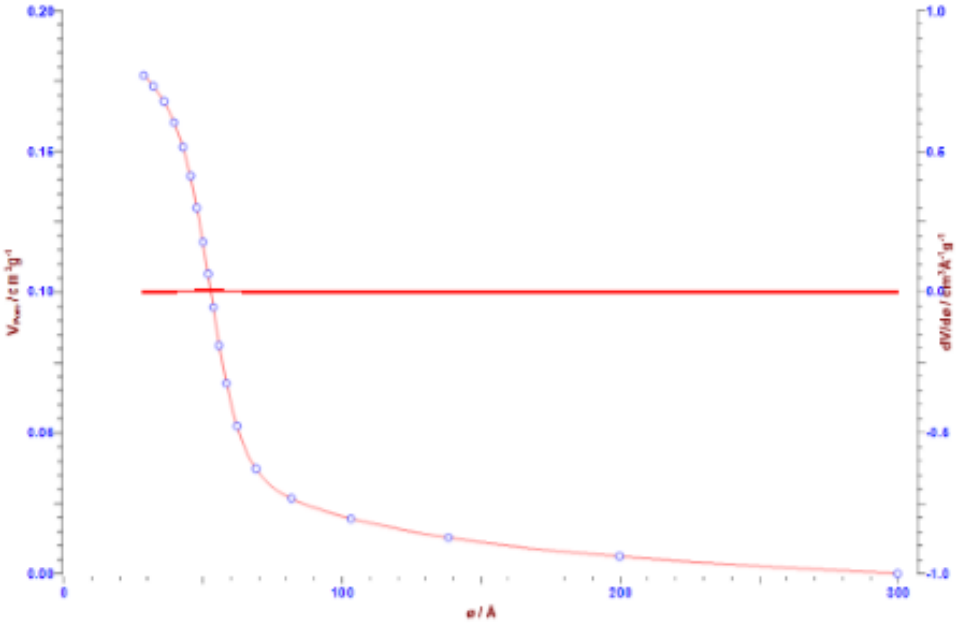

Calculations used Desorption Branch from p/p^0 0.3 to 0.95
with standard isotherm: Universal (Harkins,Jura)
from literature: ASTM Standards Designation: D 4641-87

Calculation with a molecular area of	16.2 $Å^2$
molecular weight of	28.01 g/mol
liquid density of	0.8086 g cm^{-3}
and surface tension of	8.85 Dyne cm^{-1}
Median pore diameter	54.574 Å
Maximum pore diameter	52.632 Å
Cumulative pore volume	0.177 cm^3g^{-1}
Cumulative pore area	127.11 m^2g^{-1}

Micropores (Horvath and Kawazoe)

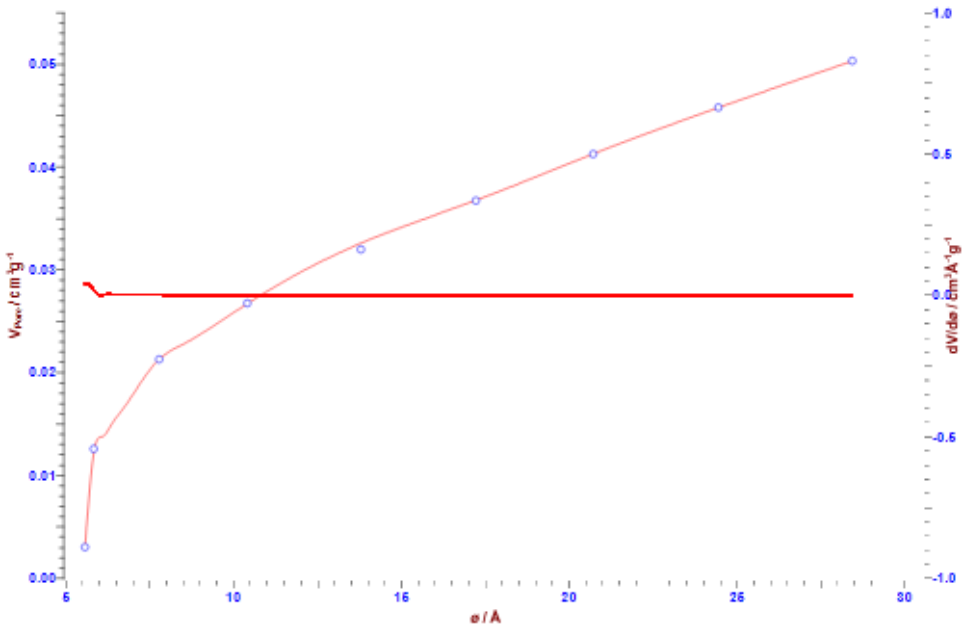

Calculations from p/p^0 0 to 0.35

with potential function: Nitrogen on Graphite @77.3 K
from literature: G. Horvath, K. Kawazoe, J. Chem. Eng. Japan, 16, 6(1983), 470-475

Calculation with a molecular area of	16.2 $Å^2$
molecular weight of	28.01 g/mol
and liquid density of	0.8086 g cm^{-3}
Median pore diameter	9.4957 Å
Maximum pore diameter	6.2818 Å
Cumulative pore volume	0.0503 cm^3g^{-1}
Cumulative pore area	100.99 m^2g^{-1}